

# Shear stress-driven flow: the state space of near-wall turbulence as $Re_\tau \rightarrow \infty$

Patrick Doohan<sup>1,†</sup>, Ashley P. Willis<sup>2</sup> and Yongyun Hwang<sup>1</sup>

<sup>1</sup>Department of Aeronautics, Imperial College London, London SW7 2AZ, UK

<sup>2</sup>School of Mathematics and Statistics, University of Sheffield, Sheffield S3 7RH, UK

(Received 1 October 2018; revised 7 June 2019; accepted 7 June 2019;  
first published online 11 July 2019)

An inner-scaled, shear stress-driven flow is considered as a model of independent near-wall turbulence as the friction Reynolds number  $Re_\tau \rightarrow \infty$ . In this limit, the model is applicable to the near-wall region and the lower part of the logarithmic layer of various parallel shear flows, including turbulent Couette flow, Poiseuille flow and Hagen–Poiseuille flow. The model is validated against damped Couette flow and there is excellent agreement between the velocity statistics and spectra for the wall-normal height  $y^+ < 40$ . A near-wall flow domain of similar size to the minimal unit is analysed from a dynamical systems perspective. The edge and fifteen invariant solutions are computed, the first discovered for this flow configuration. Through continuation in the spanwise width  $L_z^+$ , the bifurcation behaviour of the solutions over the domain size is investigated. The physical properties of the solutions are explored through phase portraits, including the energy input and dissipation plane, and streak, roll and wave energy space. Finally, a Reynolds number is defined in outer units and the high- $Re$  asymptotic behaviour of the equilibria is studied. Three lower branch solutions are found to scale consistently with vortex–wave interaction (VWI) theory, with wave forcing localising around the critical layer.

**Key words:** Turbulent flows, nonlinear dynamical systems

## 1. Introduction

There is an ever-growing body of experimental and numerical work on the scaling of the velocity statistics and spectra of wall-bounded turbulent flow, in both channel and pipe geometries as well as the flat-plate boundary layer. Closest to the wall, where viscous effects are dominant, the kinematic viscosity  $\nu$  and local shear stress define the friction velocity  $u_\tau$  and the viscous length scale  $\delta_\nu$ . One of the key observations concerning the dynamics of the near-wall region is that of the regeneration mechanism (Hamilton, Kim & Waleffe 1995) or the self-sustaining process (Waleffe 1997). This is a quasi-cyclic, interactive process between streaks and quasi-streamwise vortices, in which the mean streamwise shear drives streak formation through the lift-up effect. The streaks subsequently break down due to normal mode instability or transient growth (Hamilton *et al.* 1995; Schoppa & Hussain 2002; Cassinelli, de Giovanetti

† Email address for correspondence: [patrick.doohan15@imperial.ac.uk](mailto:patrick.doohan15@imperial.ac.uk)

& Hwang 2017) and the resulting three-dimensional wavy structure regenerates the vortices via nonlinear mechanisms. The bursting time period of the near-wall self-sustaining process is  $T^+ \approx 200\text{--}300$  (Hamilton *et al.* 1995; Jiménez *et al.* 2005), where the superscript  $+$  denotes the viscous scaling. In addition, it has been shown that there is a lower bound to the streamwise and spanwise dimensions of the computational domain in which turbulence can be sustained (Jiménez & Moin 1991). The dimensions of the minimal unit, which also scale in inner units, are  $\lambda_x^+ \approx 250\text{--}350$  and  $\lambda_z^+ \approx 100$ , consistent with the characteristic spacing of near-wall streaks (Robinson 1991). Furthermore, it has been observed that the near-wall self-sustaining process operates independently of the outer flow and survives even when the outer structures are artificially quashed (Jiménez & Pinelli 1999). The statistics and spectra of the independent near-wall flow have been compared to that of the global flow in several previous studies (Jiménez, Del Alamo & Flores 2004; Hwang 2013). In particular, in the absence of the larger structures, the velocity statistics and spectra scale in inner units throughout the near-wall region (Hwang 2013).

Above the near-wall region, the flow can be decomposed into the logarithmic layer and the wake layer, the latter of which is dominated by inertial effects. The characteristic length scale in the logarithmic layer is  $y$ , the distance from the wall. This scaling argument was formalised in the attached eddy hypothesis (Townsend 1980), in which it was proposed that the size of the coherent structures populating the entire logarithmic layer was proportional to the distance between the eddy centre and the wall. Townsend also postulated that these coherent structures were statistically self-similar with respect to the given length scale. There has been a growing body of evidence in support of Townsend's theory, including the linear growth of the spanwise correlation length scale with distance from the wall (Tomkins & Adrian 2003), the logarithmic dependence of the turbulence intensities of the wall-parallel velocity components (Marusic *et al.* 2013) and the self-similarity of structures of various spanwise length scales in the logarithmic layer (Hwang 2015). Above the logarithmic layer, the velocity field structures and statistics scale in outer units, including large-scale motions (Kovasznay, Kibens & Blackwelder 1970) and very-large-scale motions (Kim & Adrian 1999). It has been demonstrated that the coherent structures of the logarithmic and wake layers bear a self-sustaining process remarkably similar to that of the near-wall region (Hwang & Cossu 2010; Hwang & Bengana 2016), based on the interaction between streaks and quasi-streamwise vortices. Therefore, it appears that wall-bounded turbulence is organised into a hierarchy of self-sustaining coherent structures, each of which is self-similar with respect to the characteristic inner or outer length scale. Furthermore, it is worth mentioning that the coherent structures populating the logarithmic and wake layers reach the near-wall region (Hutchins & Marusic 2007; Mathis, Hutchins & Marusic 2009; Hwang 2013; Talluru *et al.* 2014; Agostini & Leschziner 2016) and contribute significantly to the near-wall spectra at long wavelengths through scale interaction processes (Hwang 2016; Cho, Hwang & Choi 2018). These features, consistent with Townsend's theory, breach the inner scaling of the near-wall region (Marusic, Baars & Hutchins 2017) and result in the logarithmic growth of the near-wall turbulence intensities of the wall-parallel velocity components with Reynolds number (Marusic & Kunkel 2003).

The logarithmic layer can be further partitioned into lower and upper parts, depending on the relative strength of the viscous effects. The lower part, dominated by the viscous effects of the wall, is often called the 'mesolayer' (Long & Chen 1981; Afzal 1982, 1984; Sreenivasan & Sahay 1997; Wei *et al.* 2005), which has been

classified using the mean momentum equation. Assuming a logarithmic mean velocity profile, it has been shown that the inner-scaled wall-normal location of maximum Reynolds stress scales with the friction Reynolds number as  $y^+ \sim \sqrt{Re_\tau}$  (Long & Chen 1981; Sreenivasan & Sahay 1997; Wei *et al.* 2005), below which the viscous wall effects are not negligible. The mesolayer can therefore be more generally interpreted as the layer of fluid above the wall that scales in inner units, encompassing the entire near-wall region. Furthermore, the extent of the mesolayer increases as the friction Reynolds number increases and the flow variables scale in inner units at longer and longer wavelengths. This has been corroborated by the examination of the spectra of high- $Re$  direct numerical simulations and the computation of optimal perturbations with a linear theory (Hwang 2016). Therefore, if the domain size is fixed in inner units, all flow variables will also scale in inner units at a sufficiently large value of  $Re_\tau$  and the near-wall contribution of the structures larger than the given domain size will be excluded.

In light of this evidence, the aim of the current study is to design and validate a model of independent near-wall turbulence at infinitely large friction Reynolds number, with regard to its location within the mesolayer. The Navier–Stokes equations are rescaled in inner units based on the kinematic viscosity and the friction velocity of the ‘turbulent state’, denoted by  $u_{\tau,r}$ . Consequently, the only model parameters are the inner-scaled computational domain dimensions ( $L_x^+$ ,  $L_y^+$ ,  $L_z^+$ ), which remain finite even as  $Re_\tau \rightarrow \infty$ . At the upper boundary, a horizontally uniform shear stress is applied to maintain uniform total shear stress across the entire domain, while removing any structures above this point. At the lower boundary, a no-slip boundary condition is imposed, the distinguishing feature from previous studies in which near-wall turbulence was regarded as uniform shear flow turbulence (Lee, Kim & Moin 1990; Sekimoto, Dong & Jiménez 2016). Indeed, it has been shown recently that the statistics of near-wall turbulence are considerably different from those of uniform shear flow turbulence (Yang, Willis & Hwang 2018). The key feature of this model is that it is applicable to various parallel shear flows at sufficiently large friction Reynolds number. In this limit, the governing equations of turbulent Couette flow, Poiseuille flow and Hagen–Poiseuille flow are identical because they are essentially approximated by wall-bounded shear flow around a linear base flow. For the same reason, the model would describe the universal dynamics of the mesolayer in the absence of outer flow, as long as the domain size in all spatial directions is suitably defined.

As a first step towards studying the universal mesolayer dynamics, the well-known minimal unit of near-wall turbulence (Jiménez & Moin 1991) is considered in the present study, in which the self-sustaining process at the given inner scale is well isolated. In such a small domain, the turbulent flow is fully correlated in the streamwise and spanwise directions, and the flow dynamics is largely temporal. This contrasts with turbulence in extended domains, in which the spatial and temporal dynamics are important (see Barkley (2016) for this issue in transitional flows). Therefore, under these circumstances, the most suitable approach to analyse the shear stress-driven model is with the concepts of dynamical systems theory. The temporal evolution of a turbulent velocity field, governed by the Navier–Stokes equations, can be represented by a chaotic trajectory of an infinite dimensional dynamical system. The dynamical systems approach to turbulence emerged with the computation of the first relative equilibrium solutions (Nagata 1990; Waleffe 1998, 2001, 2003) and periodic orbits (Kawahara & Kida 2001) in channel flow. The computation of invariant solutions and their linear stability analysis allows for the construction of

the state space of turbulence, within which the turbulent trajectory is confined. The laminar flow is the trivial equilibrium solution, whose linear stability may depend on the Reynolds number (Orszag 1971; Romanov 1973). The stability boundary of the laminar flow, which separates initial conditions that relaminarise from those that become fully turbulent, is referred to as the edge (Skufca, Yorke & Eckhardt 2006; Schneider, Eckhardt & Yorke 2007; Schneider *et al.* 2008) and plays a fundamental role in structuring the state space of turbulence. The computation of invariant solutions of the Navier–Stokes equations has allowed for a simplified analysis of a number of physical processes, including an equilibrium self-sustaining process (Waleffe 1998), the self-similarity of equilibria localised in the wall-normal direction (Eckhardt & Zammert 2018) and the high- $Re$  inner-scaling of wall-attached equilibria (Yang, Willis & Hwang 2019).

In order to study the dynamics of mesolayer turbulence, a near-wall flow domain similar in size to the minimal unit is analysed from a dynamical systems perspective. The edge and several invariant solutions are computed, and various phase portraits explored. While invariant solutions have been reported in previous studies with a damping technique to isolate the near-wall dynamics (Jiménez & Simens 2001; Jiménez *et al.* 2005), most of the solutions presented here are new. In addition, the invariant solutions of the shear stress-driven model are valid for a multitude of parallel shear flow configurations at sufficiently large friction Reynolds number. It must also be pointed out that shear stress-driven flow is employed as a model of wind blowing over a body of water, resulting in flow structures such as Langmuir circulation (Faller 1971; Leibovich 1983; Thorpe 2004). Hence, the invariant solutions presented here are also relevant in physical oceanography. The bifurcation behaviour of the solutions over the domain size is investigated to establish connections between different solutions and to examine their physical properties. Finally, a Reynolds number is defined in outer units and the high- $Re$  asymptotic behaviour of the equilibria is analysed to link to known high Reynolds number theories (Hall & Sherwin 2010).

## 2. Near-wall turbulence as $Re_\tau \rightarrow \infty$

### 2.1. Model formulation

The flow considered is that of an incompressible fluid in a rectangular domain with dimensions  $(L_x, L_y, L_z)$ , where  $x, y, z$  or  $x_1, x_2, x_3$  represent the streamwise, wall-normal and spanwise coordinates, respectively. The corresponding velocity components are denoted by  $u, v, w$  or  $u_1, u_2, u_3$  and time is denoted by  $t$ . A solid wall is located at the lower boundary of the domain at  $y = 0$ . Given the kinematic viscosity  $\nu$  and the fluid density  $\rho$ , the instantaneous wall shear stress is defined as

$$\tau_w(t) = \rho \nu \left\langle \left. \frac{\partial u}{\partial y} \right|_{y=0} \right\rangle_{x,z}, \tag{2.1}$$

where  $\langle \cdot \rangle_{x,z}$  denotes the average in the streamwise and spanwise directions. The wall shear stress of the ‘turbulent state’,  $\overline{\tau}_w$ , is subsequently obtained from a full simulation, where  $\overline{\cdot}$  denotes the average in time while the flow remains turbulent. The reference friction velocity is defined as  $u_{\tau,r} = \sqrt{\overline{\tau}_w/\rho}$  and the viscous length scale is then defined as  $\delta_\nu = \nu/u_{\tau,r}$ . Using  $\delta_\nu$  as the characteristic length scale and  $u_{\tau,r}$  as the characteristic velocity scale, the model is formulated in inner units with the velocity field  $\mathbf{u}^+ = (u^+, v^+, w^+) = (u, v, w)/u_{\tau,r}$ , spatial coordinates  $\mathbf{x}^+ = (x^+, y^+, z^+) = (x, y, z)/\delta_\nu$  and time  $t^+ = tu_{\tau,r}^2/\nu$ . A diagram of the flow geometry is shown in figure 1.

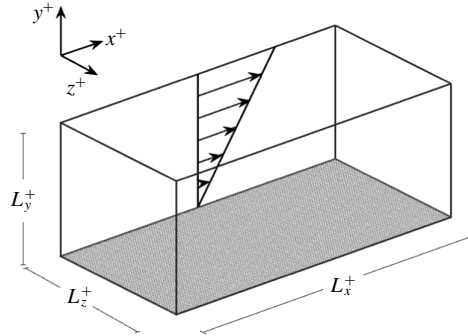


FIGURE 1. Flow geometry of the shear stress-driven model.

Employing the Reynolds decomposition, the velocity field can be expressed in terms of the mean and fluctuating components

$$\mathbf{u}^+(\mathbf{x}^+, t^+) = \mathbf{U}^+(y^+) + \mathbf{u}'^+(\mathbf{x}^+, t^+), \quad (2.2)$$

where  $\mathbf{U}^+(y^+) = (U^+(y^+), 0, 0) = (\overline{\langle u^+ \rangle}_{x^+, z^+}, 0, 0)$  and  $\mathbf{u}'^+ = (u'^+, v'^+, w'^+)$ . In channel flows, the turbulent mean and fluctuating velocity components satisfy the equations

$$\frac{dU^+}{dy^+} - \overline{\langle u'^+ v'^+ \rangle}_{x^+, z^+} = 1 - \frac{y^+}{Re_\tau}, \quad (2.3)$$

$$\begin{aligned} \mathbf{u}'^+_{,t^+} + (\mathbf{U}^+ \cdot \nabla) \mathbf{u}'^+ + (\mathbf{u}'^+ \cdot \nabla) \mathbf{U}^+ &= -\nabla p'^+ + \nabla^2 \mathbf{u}'^+ - (\mathbf{u}'^+ \cdot \nabla) \mathbf{u}'^+ \\ &\quad + \overline{\langle (\mathbf{u}'^+ \cdot \nabla) \mathbf{u}'^+ \rangle}_{x^+, z^+}, \end{aligned} \quad (2.4)$$

where  $p'^+$  is the pressure fluctuation and the  $-y^+/Re_\tau$  term is derived from the imposed pressure gradient (e.g. Townsend 1980). Within the mesolayer, the wall-normal coordinate satisfies the relation  $y^+ \sim \sqrt{Re_\tau}$  (Sreenivasan & Sahay 1997; Wei *et al.* 2005). Therefore, as  $Re_\tau \rightarrow \infty$ , the  $-y^+/Re_\tau$  term will vanish provided that  $L_y^+ \sim \sqrt{Re_\tau}$ . For parallel wall-bounded flows more generally, any terms in the mean momentum equation that are associated with the given flow geometry must vanish in the limit of  $Re_\tau \rightarrow \infty$ . The model is then governed by the following momentum equations for the turbulent mean and fluctuating components,

$$\frac{dU^+}{dy^+} - \overline{\langle u'^+ v'^+ \rangle}_{x^+, z^+} = 1, \quad (2.5)$$

$$\begin{aligned} \mathbf{u}'^+_{,t^+} + (\mathbf{U}^+ \cdot \nabla) \mathbf{u}'^+ + (\mathbf{u}'^+ \cdot \nabla) \mathbf{U}^+ &= -\nabla p'^+ + \nabla^2 \mathbf{u}'^+ - (\mathbf{u}'^+ \cdot \nabla) \mathbf{u}'^+ \\ &\quad + \overline{\langle (\mathbf{u}'^+ \cdot \nabla) \mathbf{u}'^+ \rangle}_{x^+, z^+}. \end{aligned} \quad (2.6)$$

At the lower boundary of the domain, a no-slip condition is imposed to represent the stationary wall,

$$\mathbf{u}^+|_{y^+=0} = \mathbf{0}, \quad (2.7)$$

whereas at the upper boundary, a horizontally uniform shear stress is applied. The uniform shear stress condition at the upper boundary is implemented such that the bulk

flow rate across the domain is maintained during simulations. For this purpose, the instantaneous bulk velocity is defined as  $U_b^+(t^+) = \langle u^+(x^+, y^+, z^+, t^+) \rangle_{x^+, y^+, z^+}$  ( $\langle \cdot \rangle_{x^+, y^+, z^+}$  denotes the volume average) and the laminar bulk velocity is denoted by  $U_0^+$ . Then, the streamwise boundary condition is expressed as

$$\frac{\partial u^+}{\partial y^+} \Big|_{y^+=L_y^+} (t^+) = \left\langle \frac{\partial u^+}{\partial y^+} \Big|_{y^+=0} \right\rangle_{x^+, z^+} (t^+) + C^+(U_0^+ - U_b^+(t^+)), \quad (2.8)$$

where  $C^+$  is a tuning constant that maintains  $U_b^+(t^+)$  close to  $U_0^+$  during simulations. Given that the fluctuation of  $U_b^+(t^+)$  about  $U_0^+$  is kept to a minimum, the flow is largely independent of the value of  $C^+$  but  $C^+ \approx 0.28$  is the value used throughout the present study. Since  $\overline{U_b^+(t^+)} = U_0^+$ , equation (2.8) implies that the time-averaged total shear stress (i.e. the sum of molecular and Reynolds stresses) is uniform across the entire domain as long as the wall-normal velocity at the upper boundary is zero, ensuring that the mean momentum equation (2.5) is satisfied. During the simulations of the present study,  $U_0^+ - U_b^+(t^+)$  has indeed been found to be very small, indicating that only a very small amount of compensation at the upper boundary is required at each time step to maintain  $U_b^+(t^+)$  close to  $U_0^+$ . This technique is very similar to that used to maintain constant mass flux in pressure-driven channel flow. At the upper boundary of the domain, impermeability and stress-free conditions are imposed for the wall-normal and spanwise velocity components respectively, namely

$$v^+|_{y^+=L_y^+} = 0, \quad \text{and} \quad \frac{\partial w^+}{\partial y^+} \Big|_{y^+=L_y^+} = 0, \quad (2.9a, b)$$

ensuring zero Reynolds stress at the upper boundary. The upper boundary conditions of the model may be considered *ad hoc*, however, such conditions are required to ensure that the structures of the logarithmic and wake layers are safely removed. Periodic boundary conditions are imposed in both the streamwise and spanwise directions. The numerical simulations in this work were performed with the diablo Navier–Stokes solver (Bewley 2014). This code uses spectral methods with a 2/3 dealiasing rule in the streamwise & spanwise directions and a second-order finite difference scheme in the wall-normal direction, which has been verified extensively (e.g. Hwang 2013).

Several notable features of the present model must also be mentioned. Firstly, equation (2.6) does not seem to contain any explicit control parameter, such as a Reynolds number. This is essentially because the equations of motion are normalised by the viscous length scale  $\delta_v$  and reference friction velocity  $u_{\tau,r}$ . Under this rescaling, the velocity field is governed by the unit Reynolds number Navier–Stokes equations (2.6). The inner-scaled flow variables are  $O(1)$  quantities even in the limit of  $Re_\tau \rightarrow \infty$ . However, this does not imply that the equations do not have a control parameter. In this case, the domain dimensions (i.e.  $(L_x^+, L_y^+, L_z^+)$ ) are the main control parameters, as long as they are finite. In particular, the spanwise width of the domain can be used to determine the expected multiplicity (or levels in the hierarchy) of integral length scales. For example, if  $L_z^+ \simeq 100$ , it will only include the near-wall energy-containing structures at a single integral length scale (Jiménez & Moin 1991). If  $L_z^+ \simeq 200$ , it will include two integral length scales (i.e.  $\lambda_z^+ \simeq 100, 200$ ) due to the spanwise periodic boundary condition. Secondly, it must be emphasised that (2.5) only governs



the turbulent mean velocity field. The laminar state (and other invariant solutions) satisfy

$$\frac{dU^+}{dy^+} - \overline{\langle u'^+v'^+ \rangle}_{x^+,z^+} = \Delta^+, \quad (2.10)$$

where  $\Delta^+ = dU^+/dy^+|_{y^+=0}$  is the wall shear rate of the corresponding solution, which is smaller than unity in the laminar case. However, the present model ensures that the base flow is a uniform shear flow – this can be easily checked by setting the Reynolds stress in (2.10) to zero, with solution  $U^+ = \Delta^+y^+$ . The laminar bulk velocity is then  $U_0^+ = \Delta^+L_y^+/2 \approx 13.89$ . This implies that the model would be valid in the region close to the wall, where the base flow can be approximated by a uniform shear flow. This also indicates that the base flow in the mesolayer is a uniform shear flow, explaining why the description by (2.5) and (2.6) would be universal for any parallel wall-bounded shear flow. Finally, it is evident that the crucial issue in the use of the present model is the use of the upper boundary condition (2.8), which could potentially affect the region that is to be studied. For this reason, the model is first carefully validated in § 2.2.

## 2.2. Validation of the shear stress-driven flow model

The shear stress-driven flow model presented in the previous subsection must now be evaluated, and the velocity statistics and spectra compared to that of independent near-wall turbulence. The obvious benchmark for the model is near-wall Couette flow, which exactly satisfies (2.5) and (2.6) at all Reynolds numbers. In order to isolate the near-wall flow, a damping function is introduced to the system, which quashes turbulent fluctuations above a fixed wall-normal height. The damping function employed is

$$\mu^+(y^+) = \frac{\mu_0^+}{2} \left[ 1 + \tanh \left( 10 \left( \left( \frac{y^+}{y_0^+} \right)^2 - 1 \right) \right) \right], \quad (2.11)$$

similar to that used by Jiménez & Pinelli (1999). Here,  $\mu_0^+$  denotes the damping amplitude and  $y_0^+$  denotes the damping height, such that  $\mu^+(y^+)$  tends to the constant  $\mu_0^+$  above  $y_0^+$  and decays rapidly to zero below this point. Above the damping height, the turbulent fluctuations are damped onto the mean flow, hence the system is governed by the equations

$$\mathbf{u}_{t^+}^+ + (\mathbf{u}^+ \cdot \nabla) \mathbf{u}^+ = -\nabla p^+ + \nabla^2 \mathbf{u}^+ - \mu^+(y^+) (\mathbf{u}^+ - \langle \mathbf{u}^+ \rangle_{x^+,z^+}). \quad (2.12)$$

The value of the damping height is chosen to be  $y_0^+ \approx 95$  so that the near-wall flow is unaffected. The value of the damping amplitude must be sufficiently high to kill all turbulent fluctuations above the damping height and it was found that  $\mu_0^+ \approx 0.33$  achieves appropriate results. Since the damping function kills Reynolds stresses above the damping height, the kinematic viscosity must increase in line with the Fukagata–Iwamoto–Kasagi identity (Fukagata, Iwamoto & Kasagi 2002) to maintain similar inner-scaled domain dimensions. To compare both flow configurations, a long streamwise domain length of  $L_x^+ \approx 3000$  is chosen so that the longest streaky structures are resolved. However, the spanwise domain width is chosen to be close to that of the minimal unit,  $L_z^+ \approx 110$ , so as to remove the wider structures of the outer

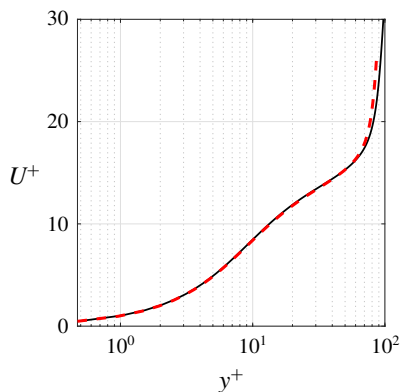


FIGURE 2. (Colour online) Mean streamwise velocity,  $U^+(y^+)$ , of the shear stress-driven flow model (red dashed line), plotted against that of damped Couette flow (black solid line).

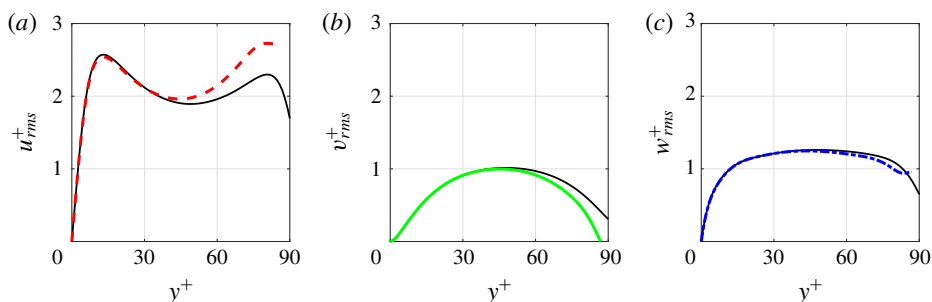


FIGURE 3. (Colour online) Root mean squared velocity of the shear stress-driven flow model; (a)  $u_{rms}^+$  (red dashed line), (b)  $v_{rms}^+$  (green solid line) and (c)  $w_{rms}^+$  (blue dash-dotted line), plotted against that of damped Couette flow (black solid lines).

---

Case	$L_x^+$	$L_y^+$	$L_z^+$	$N_x$	$N_y$	$N_z$	$y_0^+$
SSDF	2900	87	106	300	105	32	n/a
DCF	3042	146	111	300	161	32	95

---

TABLE 1. Simulation parameters of the shear stress-driven flow model and damped Couette flow.

flow. The shear stress-driven flow model is denoted by SSDF and damped Couette flow by DCF, and the simulation parameters are displayed in table 1. All statistics presented here were computed over a time period of  $T^+ > 35\,000$ .

The mean streamwise velocity profile of the shear stress-driven flow model compared to that of damped Couette flow is shown in figure 2. There is excellent agreement between the two flow configurations for  $y^+ < 70$  but the shear stress-driven model slightly overestimates the mean velocity above this point. The viscous sublayer features the characteristic linear profile, which is also seen near the upper boundary of the domain. Similar behaviour is observed in the root mean squared velocity statistics in figure 3. The shear stress-driven model clearly captures the near-wall



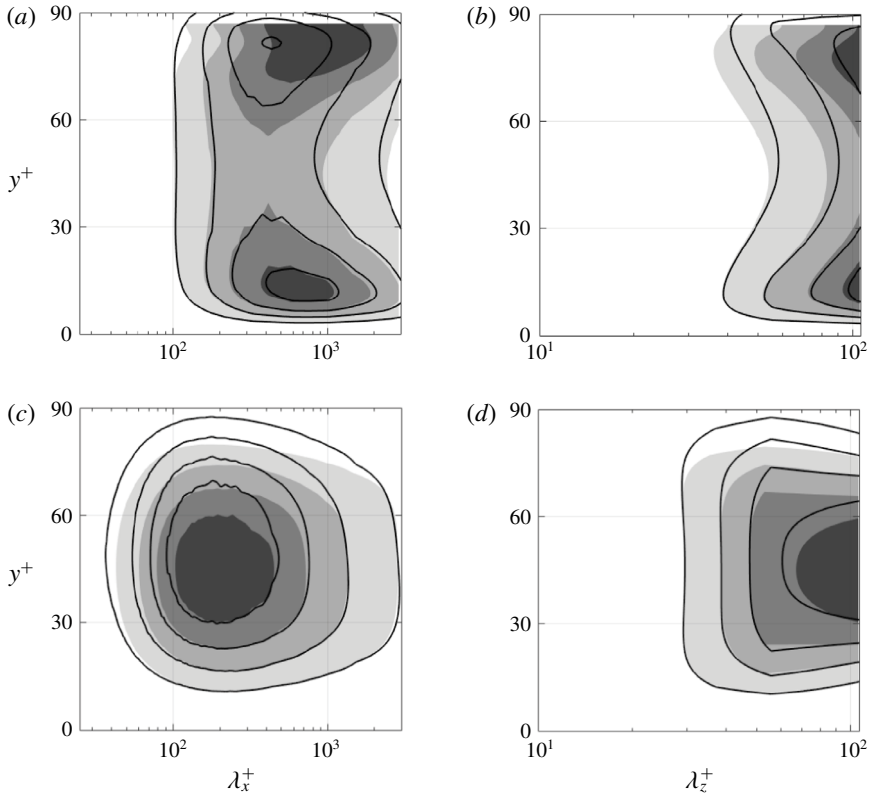


FIGURE 4. For caption see next page.

peak of the streamwise velocity fluctuation at  $y^+ \approx 12$  but again overestimates the streamwise velocity near the upper boundary. In contrast, the wall-normal and spanwise velocity fluctuations are underestimated by the shear stress-driven model near the upper boundary but show excellent agreement closer to the wall. The premultiplied one-dimensional streamwise and spanwise wavenumber spectra are shown in figure 4. As seen in the first- and second-order statistics, there is excellent agreement between the shear stress-driven model and damped Couette flow for  $y^+ < 40$ . The streamwise wavenumber spectra of the streamwise velocity shows slight excitation at longer streamwise wavelengths near the upper boundary, consonant with the previous statistical results. The spectra of the wall-normal and spanwise velocity components are also underestimated near the upper boundary. In general, the spanwise wavenumber spectra of the three velocity components and Reynolds stress show excellent agreement.

### 3. The state space of near-wall turbulence

Having introduced the shear stress-driven flow model and validated it against damped Couette flow, the task at hand is to describe near-wall turbulence from a dynamical systems perspective. To this end, the domain dimensions are fixed at  $(L_x^+ = 320, L_y^+ = 90, L_z^+ = 110)$ , slightly larger than the minimal unit in which turbulence can be sustained (Jiménez & Moin 1991). This reference domain is denoted by  $\Omega$  and its parameters are set out in table 2. The Navier–Stokes equations, subject

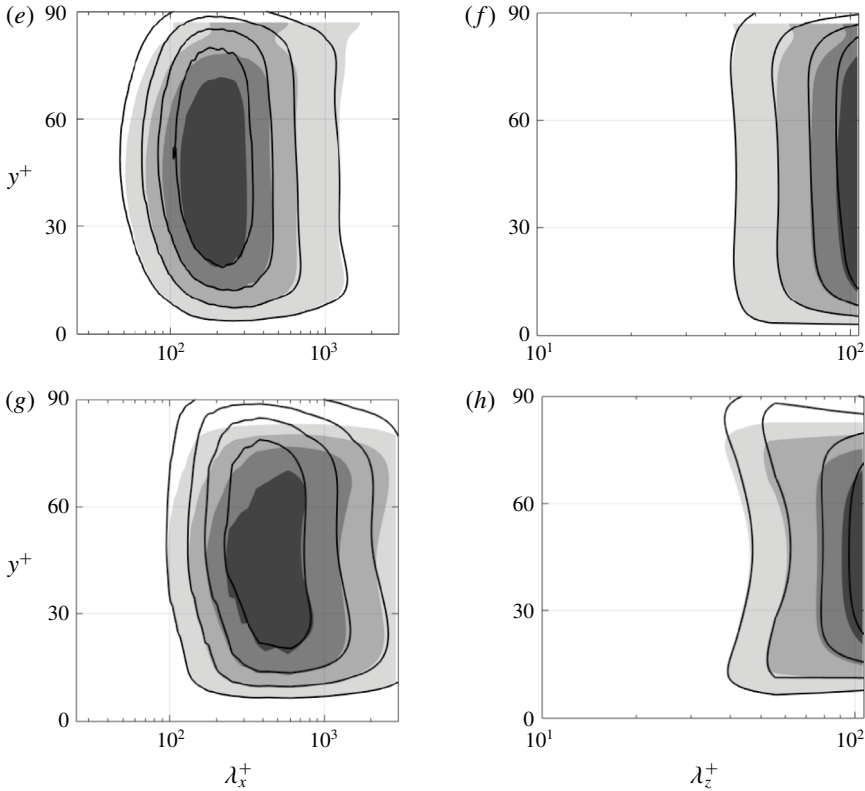


FIGURE 4 (cntd). Premultiplied one-dimensional streamwise (*a,c,e,g*) and spanwise (*b,d,f,h*) wavenumber spectra of the shear stress-driven flow model; (*a,b*) streamwise velocity, (*c,d*) wall-normal velocity, (*e,f*) spanwise velocity and (*g,h*) Reynolds stress. Isocontours of damped Couette flow are superimposed in black.

---

$L_x^+$	$L_y^+$	$L_z^+$	$N_x$	$N_y$
320	90	110	32	105

---

TABLE 2. Simulation parameters of the reference domain,  $\Omega$ .

to boundary conditions (2.7)–(2.9), are subsequently solved in the shift-reflectional subspace,

$$[u^+, v^+, w^+](x^+, y^+, z^+) = [u^+, v^+, -w^+](x^+ + L_x^+/2, y^+, -z^+), \quad (3.1)$$

to reduce the dimensionality of the turbulent state space. However, it has been shown that this symmetry does not significantly alter the statistics and dynamics of the turbulent trajectory (Hwang, Willis & Cossu 2016) since it captures the sinuous mode of streak instability, which is the dominant streak breakdown mechanism in the self-sustaining process (Hamilton *et al.* 1995; Cassinelli *et al.* 2017; de Giovanetti, Sung & Hwang 2017).

## 3.1. Edge and invariant solutions

As in the case of Couette flow, the base flow of the shear stress-driven flow model has a linear velocity profile. However, any perturbations to the base flow are subject to different boundary conditions than those of Couette flow, namely (2.8) and (2.9), hence the linear stability of the base flow is not guaranteed. A simple way to verify the linear stability of the base flow for the parameters chosen is to determine whether it is possible to compute the edge, the hyper-dimensional manifold that separates initial conditions that relaminarise from those that become fully turbulent (Skufca *et al.* 2006). In this case, the edge of  $\Omega$  is computed via bisection, in which the turbulent fluctuations of a random initial condition are rescaled so as to lie between specific laminar and turbulent thresholds. This modified velocity field is advanced in time until the transient behaviour has decayed sufficiently, denoted by time  $t_0^+$ . The edge is a fundamental feature of the state space of a parallel wall-bounded shear flow. The turbulent state space is also structured by invariant solutions, including relative equilibrium solutions and relative periodic orbits, whose stable and unstable manifolds guide nearby turbulent trajectories. Such invariant solutions are computed using the Newton–Krylov–Hookstep algorithm (Viswanath 2007, 2009; Willis, Cvitanović & Avila 2013), which has been verified extensively in Hwang *et al.* (2016). Given an initial condition  $\mathbf{u}_0^+$ , this algorithm seeks to minimise the relative error between the initial condition and its translated time-forward map

$$r = \frac{\|\mathbf{u}_0^+ - \tau(s_{x^+}, s_{z^+})f^{T^+}(\mathbf{u}_0^+)\|}{\|\mathbf{u}_0^+\|}, \quad (3.2)$$

where  $f$  denotes the Navier–Stokes propagator and  $\tau$  represents a translation of distance  $s_{x^+}$  in the streamwise direction and  $s_{z^+}$  in the spanwise direction. For periodic orbits, the value of  $T^+$  is updated at each Newton iteration from a good initial guess and the converged value becomes the time period (up to positive integer multiplication of the fundamental period). For equilibria, the choice of  $T^+$  is arbitrary but  $T^+ \approx 16$  is the value used for those computed here. All invariant solutions reported in this work satisfy  $r < 10^{-8}$ . The eigenvalues of converged solutions are subsequently computed via Arnoldi iteration.

Defining the streamwise turbulent fluctuation energy as

$$E_u^+ = \frac{1}{2} \langle (u'^+)^2 \rangle_{x^+, y^+, z^+}, \quad (3.3)$$

the edge of  $\Omega$  as a function of time is shown in figure 5. After the transient behaviour has decayed, the edge initially shows statistically stationary behaviour, from which the first relative equilibrium solution,  $EQ_{A1L}$ , was computed. However, this equilibrium solution is unstable to a gentle relative periodic orbit on the edge. In figure 5, the edge trajectory leaves the neighbourhood of the equilibrium solution and is pulled towards the periodic orbit, stabilising at later time. This periodic orbit, titled  $PO_{A0L}$ , is stable on the edge and hence it is the edge state. Therefore, the transient visit of  $EQ_{A1L}$  in figure 5 is a peculiarity of the initial condition for the bisection, since any edge trajectory in the neighbourhood of  $PO_{A0L}$  will approach it monotonically. The other invariant solutions were computed using initial conditions taken directly from the turbulent trajectory or via continuation. In total, two relative periodic orbits and thirteen relative equilibrium solutions were found in  $\Omega$ . They are distinguished into three distinct groups (A, B and C) in the following discussion and their properties are summarised in table 3.

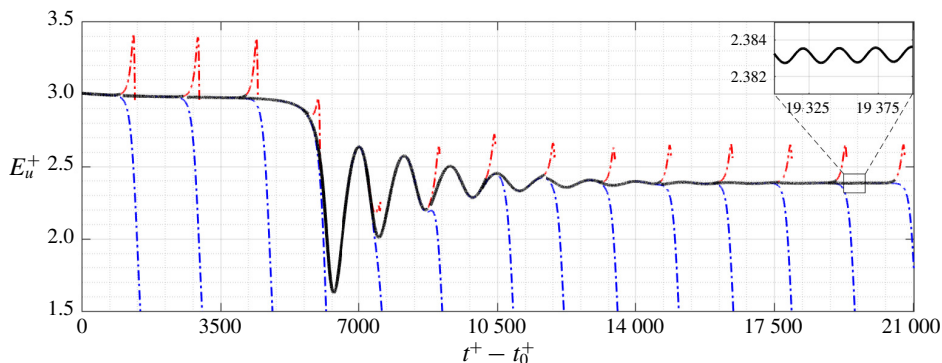


FIGURE 5. (Colour online) The edge of the reference domain  $\Omega$  (black solid line), separating initial conditions that relaminarise (blue dash-dotted lines) from those that become fully turbulent (red dash-dotted lines).  $E_u^+$  is the streamwise turbulent fluctuation energy and  $t_0^+$  is the time by which the initial transient behaviour of the edge has decayed sufficiently. The inset shows the relative periodic orbit embedded in the edge.

	$T^+$	$c_x^+$	$\Delta^+$	$I/I_l$	$E_p$	$\dim(W^u)$
$PO_{A0L}$	26.2272	14.0281	0.4053	1.3092	3.3016	1
$EQ_{A1L}$	—	16.8070	0.4019	1.1962	4.7462	3
$EQ_{A2}$	—	15.1808	0.3549	1.1325	0.5489	3
$EQ_{A3L}$	—	10.3307	0.3979	1.3600	1.8629	3
$EQ_{A4L}$	—	14.9931	0.3576	1.1423	0.8946	3
$EQ_{B5L}$	—	14.8210	1.0078	2.5056	20.0140	19
$EQ_{B3U}$	—	7.0278	0.5453	1.8650	4.0807	8
$EQ_{B4U}$	—	14.9599	0.4200	1.3195	2.5399	6
$EQ_{B6L}$	—	14.6201	0.6707	2.0041	10.7257	14
$EQ_{B6U}$	—	14.3803	0.7864	2.3703	12.6819	17
$PO_{C0U}$	25.7832	12.6168	1.1941	3.9097	14.1242	47
$EQ_{C1U}$	—	14.2457	1.5442	4.1139	23.5143	22
$EQ_{C5U}$	—	14.1047	1.6692	4.5419	23.9548	25
$EQ_{C7L}$	—	12.9620	1.2743	3.8623	10.3416	38
$EQ_{C7U}$	—	13.5580	1.6092	4.5532	13.6796	63

TABLE 3. Properties of the invariant solutions in  $\Omega$ :  $T^+$ , the time period;  $c_x^+$ , the phase speed;  $\Delta^+$ , the wall shear rate;  $I/I_l$ , the energy input normalised by that of the laminar state;  $E_p$ , the kinetic energy deviation from the laminar state;  $\dim(W^u)$ , the dimension of the unstable manifold. The  $c_x^+$ ,  $\Delta^+$ ,  $I/I_l$  and  $E_p$  values of  $PO_{A0L}$  and  $PO_{C0U}$  are averages over the period  $T^+$ .

The Group A solutions are characterised by small cross-streamwise velocity fluctuations relative to the streamwise velocity fluctuations. Velocity isosurfaces and second-order statistics are shown in figure 6. Titled  $PO_{A0L}$ ,  $EQ_{A1L}$ ,  $EQ_{A2}$ ,  $EQ_{A3L}$  and  $EQ_{A4L}$  respectively, each solution in this group is a lower branch solution (figure 9). As previously mentioned,  $PO_{A0L}$  is the edge state. It is time periodic with  $T^+ \approx 26.2$ , an order of magnitude shorter than the bursting period of near-wall turbulence (Hamilton *et al.* 1995; Jiménez *et al.* 2005), and its oscillation amplitude is very

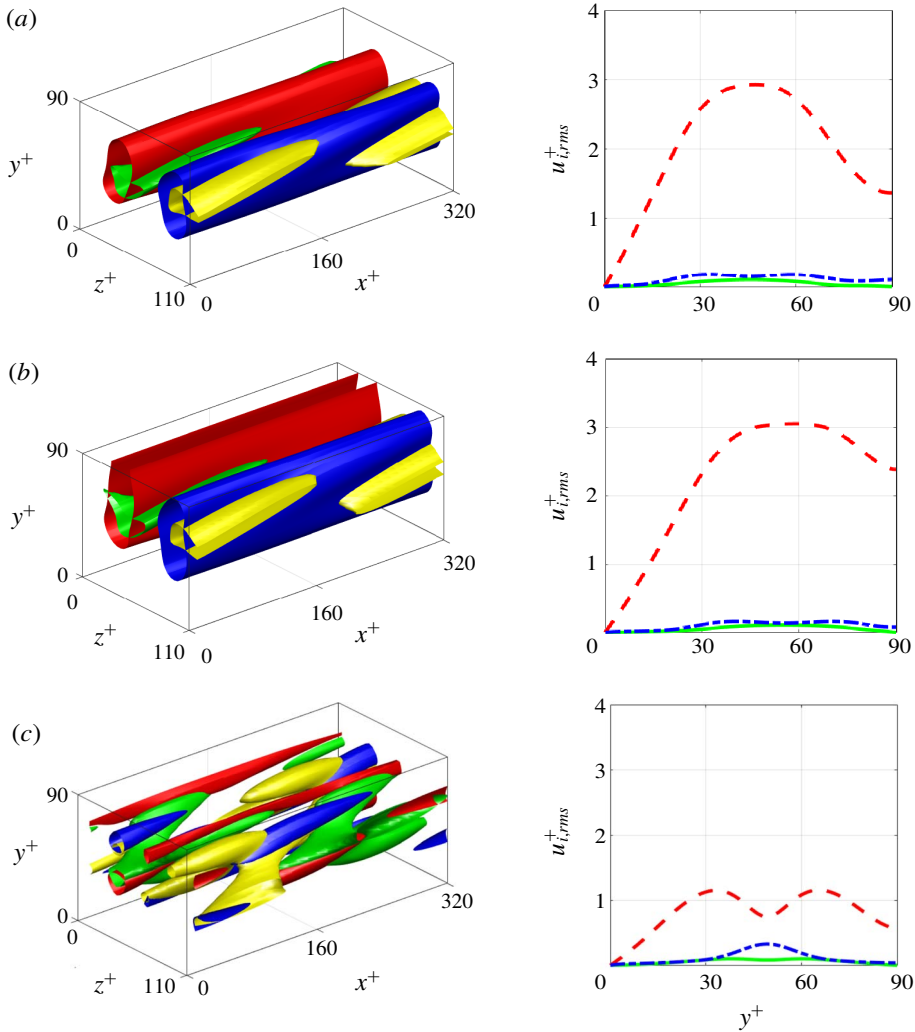


FIGURE 6. For caption see next page.

small ( $t^+ - t_0^+ \simeq 20000$  in figure 5). However, its  $E_u^+$  value is significantly different to that of  $EQ_{AIL}$  ( $t^+ - t_0^+ \simeq 0$  in figure 5), which is noticeable in the  $u_{rms}^+$  profile near the upper boundary. This periodic orbit might be related to that identified in the near-wall region of Poiseuille flow by Jiménez & Simens (2001) or to the ‘gentle’ periodic orbit on the edge in Kawahara & Kida (2001) (see also Lustro *et al.* 2019). The  $EQ_{AIL}$  state is the equilibrium solution embedded in the edge. However, it has a three-dimensional unstable manifold; one dimension representing the instability of the edge and the other two representing its instability to  $PO_{AOL}$ . It is dominated by a pair of strong streaks, flanked by weaker vortical motion. Examination of the velocity field indicates that this is presumably the stress-driven analogue of Nagata’s lower branch solution (Nagata 1990), without the shift-rotational symmetry possessed by Couette flow. If an appropriate computational domain is provided, Nagata’s lower branch solution also arises as the edge state of Couette flow (Schneider *et al.* 2008). The Group A solutions all have wall shear rates well below the turbulent mean but

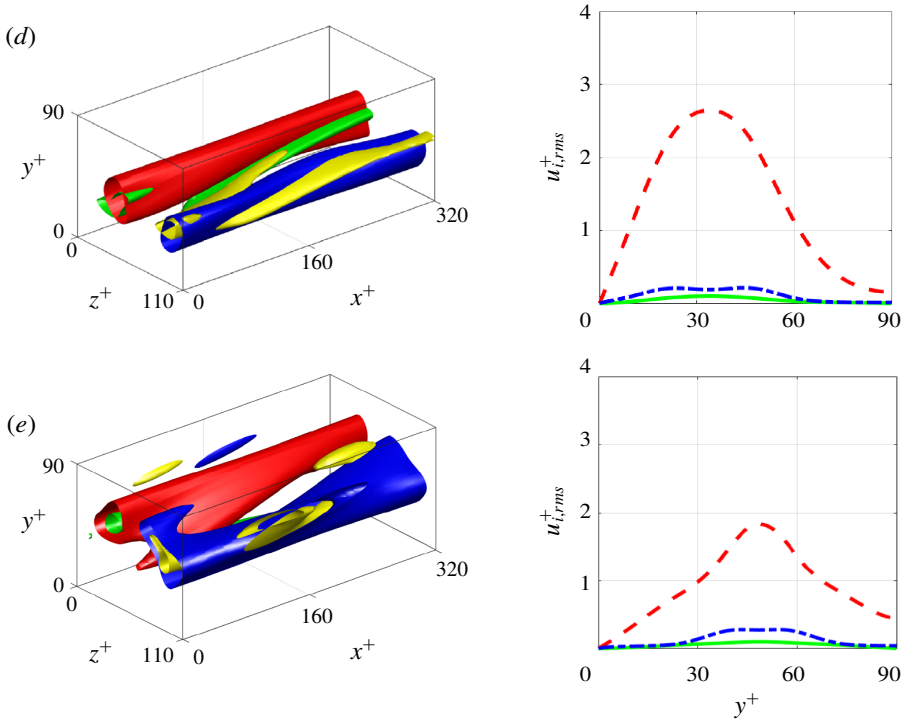


FIGURE 6 (cntd). (Colour online) Velocity field visualisation and root mean squared velocity profiles of the Group A relative periodic orbit and relative equilibrium solutions, henceforth titled  $PO_{A0L}$ ,  $EQ_{A1L}$ ,  $EQ_{A2}$ ,  $EQ_{A3L}$  and  $EQ_{A4L}$ , respectively. The red and blue surfaces represent high- and low-speed streaks; (a,b,d)  $u^+ - \langle u^+ \rangle_{x^+,z^+} = \pm 3$ , (c,e)  $u^+ - \langle u^+ \rangle_{x^+,z^+} = \pm 1.5$ . The yellow and green surfaces are iso-surfaces of wall-normal velocity;  $v^+ = \pm 0.12$ . Red dashed lines,  $u_{rms}^+$ ; green solid lines,  $v_{rms}^+$ ; blue dash-dotted lines,  $w_{rms}^+$ . The root mean squared velocity profile of  $PO_{A0L}$  is an average over the period  $T^+$ .

$EQ_{A2}$  is the equilibrium solution with the lowest drag in  $\Omega$  (table 3). In fact, it is analogous to  $EQ_7$  computed by Gibson, Halcrow & Cvitanovi (2009) and is the only solution to comprise of two pairs of streaks. The  $EQ_{A3L}$  state is a ‘wall-attached’ solution, showing clear vertical localisation and little activity near the upper boundary. It too consists of a pair of strong streaks, driven by cross-streamwise motion an order of magnitude lower. The  $EQ_{A4L}$  state is the last Group A solution and also exhibits vertical localisation, this time in the domain centre. The maximum streak value is similar to that of  $EQ_{A2}$ , hence it has the second-lowest drag in  $\Omega$ . Again, this solution possesses a Couette flow analogue, namely  $EQ_3$  computed by Gibson *et al.* (2009).

Group B comprises the equilibria whose wall shear rate values are in the vicinity of the turbulent mean, specifically  $0.41 < \Delta^+ < 1.01$  (table 3). In this sense, these solutions can be described as ‘moderately turbulent states’. In contrast to Group A, the equilibria in this group show much greater velocity field diversity, as seen in the velocity isosurfaces and second-order statistics in figure 7. This is due to the fact that both lower and upper branch solutions are present. However, the Group B equilibria are clustered together in state space, as seen in the phase portraits in figures 10 and 11. In particular, the energy input (3.5) of the solutions relative to that of the laminar state lies in the interval  $1.3 < I/I_l < 2.6$ . These equilibria are much more unstable than

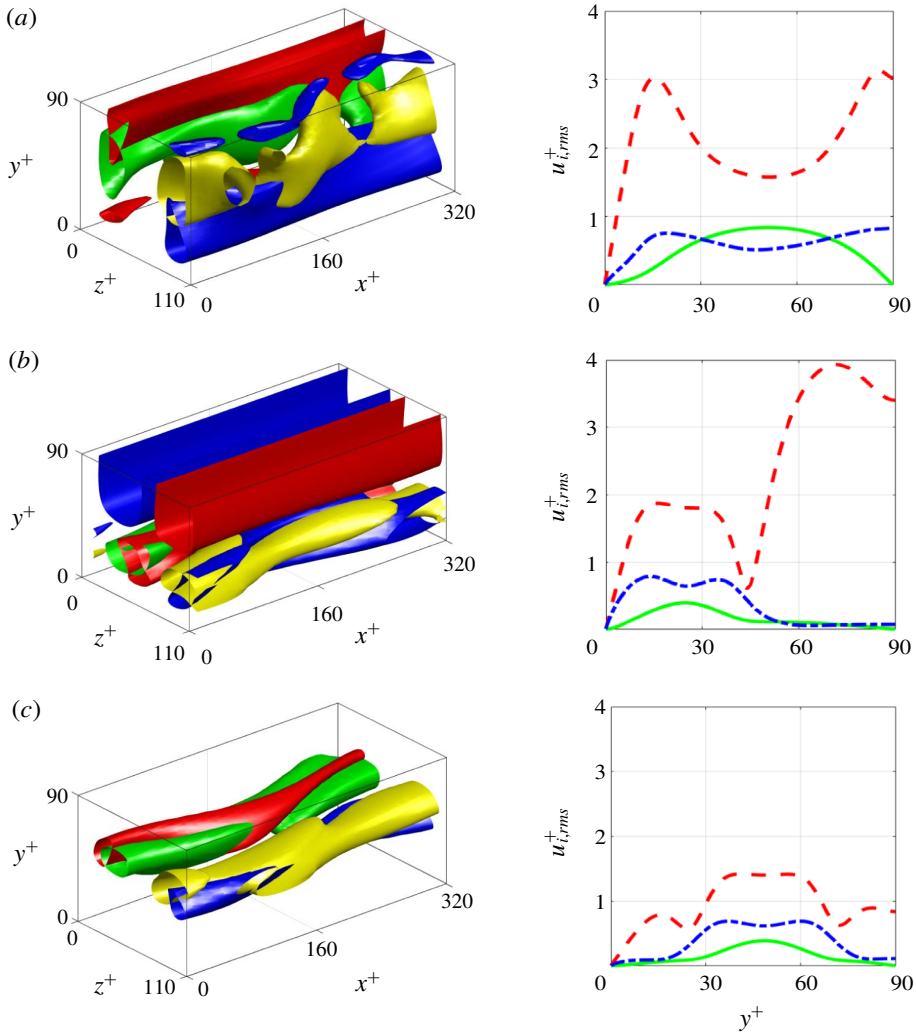


FIGURE 7. For caption see next page.

the solutions of Group A, each having an unstable manifold of dimension 6–19. The  $\mathbf{EQ}_{B5L}$  state is an equilibrium solution that bifurcates away from the  $EQ_{A1L}$  branch, just above the turning point (figure 9a). It is very similar structurally to a typical upper branch solution, with the localisation of the low-speed streak along the wall and high-speed streak along the upper boundary, except for significantly lower drag. In fact, the drag of this solution is almost exactly equal to that of the turbulent trajectory in  $\Omega$ , hence it could be argued that  $EQ_{B5L}$  represents the mean turbulent state. The  $\mathbf{EQ}_{B3U}$  state is the upper branch of the ‘wall-attached’ solution  $EQ_{A3L}$ . It consists of two distinct regions;  $y^+ < 40$ , where the cross-streamwise velocity fluctuations are of the same order as the streamwise fluctuations, and  $y^+ > 40$ , where the streamwise velocity fluctuations dominate. Correspondingly, in the velocity field visualisation (figure 7b), a pair of near-wall streaks are present together with the sustaining vortical motion, as well as a pair of energetic streaks along the upper boundary. The  $\mathbf{EQ}_{B4U}$  state is the upper branch of  $EQ_{A4L}$  and like its lower branch counterpart, it too is vertically



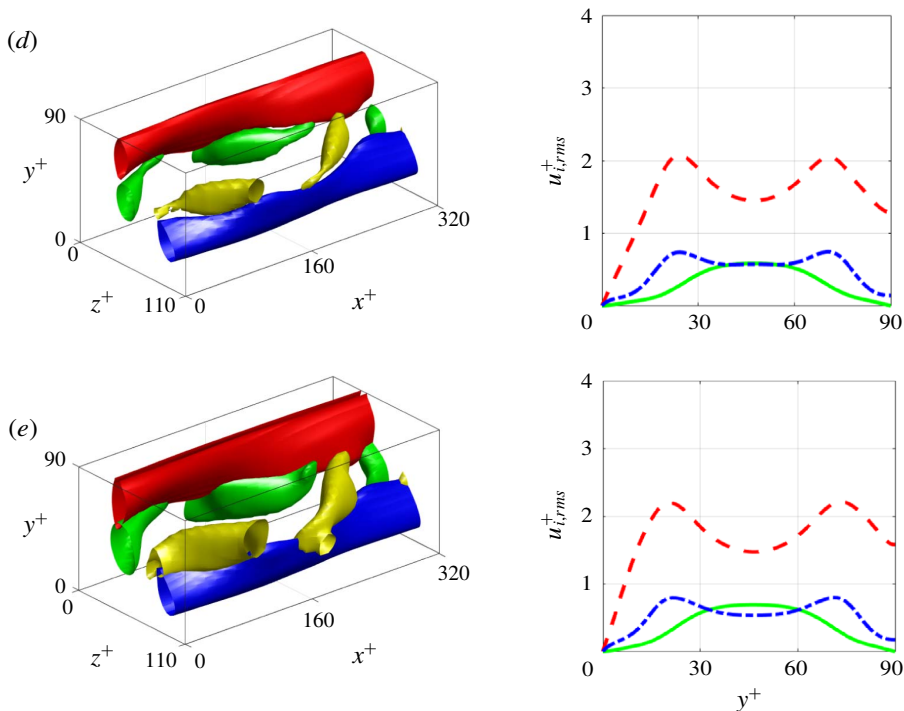


FIGURE 7 (cntd). (Colour online) Velocity field visualisation and root mean squared velocity profiles of the Group B relative equilibrium solutions, henceforth titled  $EQ_{B5L}$ ,  $EQ_{B3U}$ ,  $EQ_{B4U}$ ,  $EQ_{B6L}$  and  $EQ_{B6U}$ , respectively. The red and blue surfaces represent high and low speed streaks; (a,d,e)  $u^+ - \langle u^+ \rangle_{x^+,z^+} = \pm 3$ , (b,c)  $u^+ - \langle u^+ \rangle_{x^+,z^+} = \pm 2$ . The yellow and green surfaces are isosurfaces of wall-normal velocity; (a,d,e)  $v^+ = \pm 0.9$ , (b,c)  $v^+ = \pm 0.35$ . Red dashed lines,  $u_{rms}^+$ ; green solid lines,  $v_{rms}^+$ ; blue dash-dotted lines,  $w_{rms}^+$ .

localised in the domain centre. Both the low- and high-speed streaks exhibit wavy behaviour, resembling streak instability, and the wall-normal fluctuations are much more prominent. However, due to the wall-normal localisation, the wall shear stress remains relatively low for an upper branch solution, as for its Couette flow analogue  $EQ_4$  (Gibson *et al.* 2009). The  $EQ_{B6L}$  and  $EQ_{B6U}$  states are the last Group B solutions. A lower and upper branch pair, these equilibria are positioned quite close together in state space (figures 10 and 11). Consequently, the two solutions are very similar structurally, the only differences being a shift closer to the wall in the  $u_{rms}^+$  profile and a small increase in wall-normal velocity content.

The Group C solutions are characterised by large near-wall peaks in the streamwise velocity fluctuations, as shown in the velocity isosurfaces and second-order statistics in figure 8. Consequently, these solutions exhibit very high wall shear rates and can be described as the ‘high drag states’. In contrast to Group A and B, each of the Group C solutions has a wall shear rate greater than the turbulent mean, specifically  $\Delta^+ > 1.19$  (table 3). These solutions are also highly dissipative, with energy dissipation (3.6) relative to that of the laminar state satisfying  $D/D_l > 3.8$ . Unsurprisingly, the solutions in this group are highly unstable, with unstable manifolds of dimension 22 or greater. The  $PO_{C0U}$  state is the upper branch of  $PO_{A0L}$ , the edge state. It is also time periodic, with  $T^+ \approx 25.8$ , and its oscillation amplitude is still quite small (figures 10

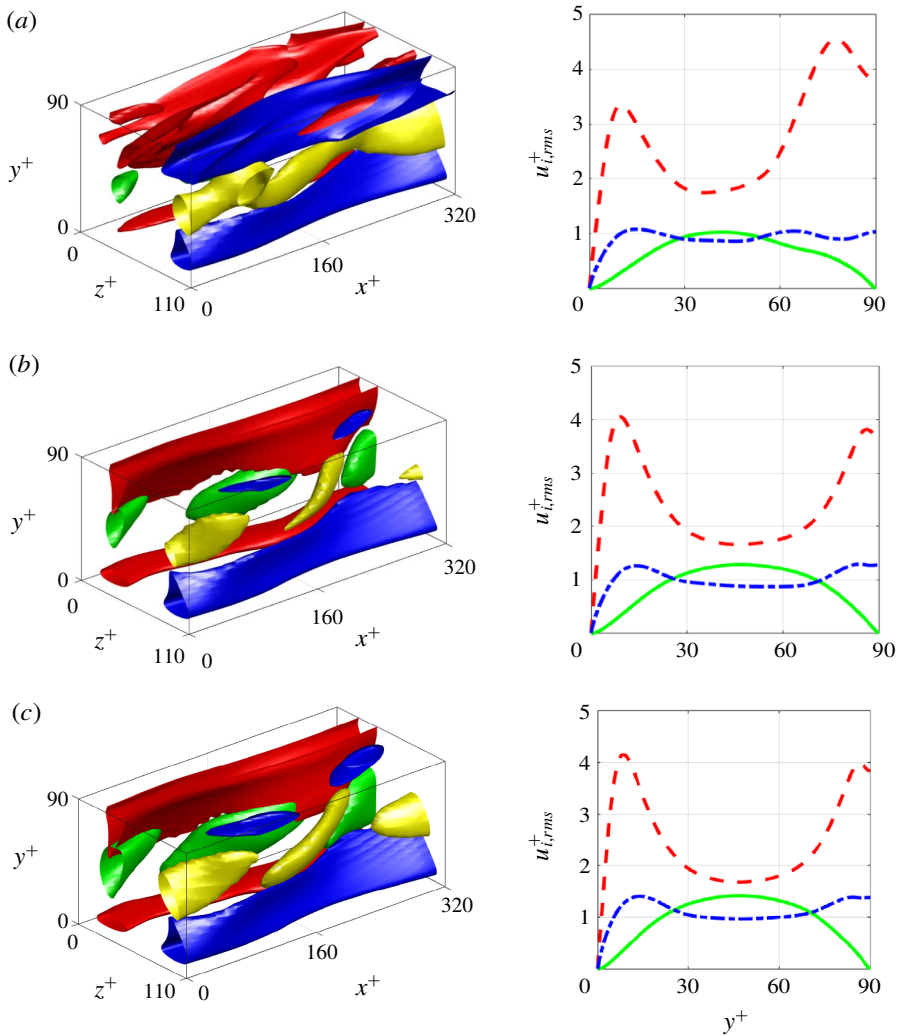


FIGURE 8. For caption see next page.

and 11). In contrast to the stability of its lower branch counterpart,  $PO_{COU}$  has a 47-dimensional unstable manifold, the second most unstable in  $\Omega$ . It features very strong streaks along the upper boundary of the domain, resulting in a skewed  $u_{rms}^+$  profile. The  $EQ_{CIU}$  state is the upper branch of  $EQ_{AIL}$ , the equilibrium solution embedded in the edge. As seen in the Group B equilibria, the low-speed streak localises along the wall and the high-speed streak localises along the upper boundary, resulting in a bimodal  $u_{rms}^+$  distribution. Again, examination of the velocity field indicates that this is presumably the stress-driven equivalent to Nagata's upper branch solution (Nagata 1990). The  $EQ_{CSU}$  state is the upper branch of  $EQ_{BSL}$ , the solution that bifurcates away from the main  $EQ_{AIL} - EQ_{CIU}$  branch (figure 9a). Structurally, it is very similar to  $EQ_{CIU}$ , except for small differences in the wall-normal velocity content. In fact,  $EQ_{CSU}$  is the solution with the highest drag in  $\Omega$  (table 3). Finally,  $EQ_{C7L}$  and  $EQ_{C7U}$  are the last Group C solutions. A lower and upper branch pair, both equilibria are characterised by very 'turbulent' velocity fields, containing high-speed streaks near

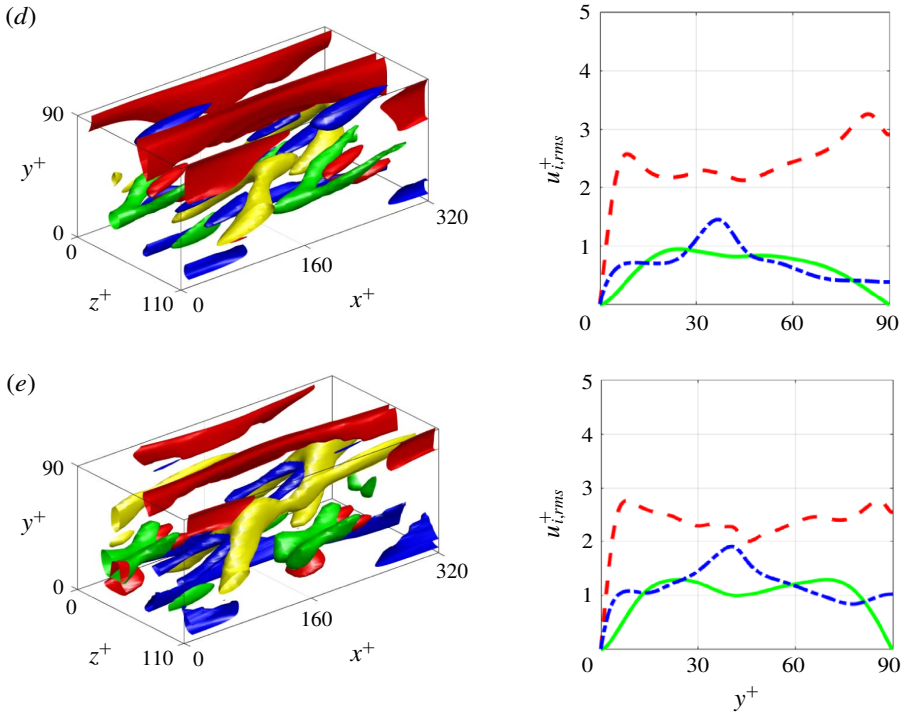


FIGURE 8 (contd). (Colour online) Velocity field visualisation and root mean squared velocity profiles of the Group C relative periodic orbit and relative equilibrium solutions, henceforth titled  $PO_{C0U}$ ,  $EQ_{C1U}$ ,  $EQ_{C5U}$ ,  $EQ_{C7L}$  and  $EQ_{C7U}$ , respectively. The red and blue surfaces represent high- and low-speed streaks;  $u^+ - \langle u^+ \rangle_{x^+,z^+} = \pm 3.75$ . The yellow and green surfaces are iso-surfaces of wall-normal velocity; (a,d)  $v^+ = \pm 1.4$ , (b,c,e)  $v^+ = \pm 1.9$ . Red dashed lines,  $u^+_{rms}$ ; green solid lines,  $v^+_{rms}$ ; blue dash-dotted lines,  $w^+_{rms}$ . The root mean squared velocity profile of  $PO_{C0U}$  is an average over the period  $T^+$ .

the upper boundary and strong vortical structures. The root mean squared velocity profiles of both solutions are quite uneven, the only pair to exhibit such behaviour. Both equilibria are extremely unstable, possessing 38- and 63-dimensional unstable manifolds respectively.

### 3.2. Bifurcation of solutions

Thus far, three distinct groups of invariant solutions of the Navier–Stokes equations have been presented. In order to establish connections between the different solutions and to analyse their physical properties, the bifurcation of solutions over the domain size is investigated. Each periodic orbit and equilibrium solution is continued to smaller and larger values of the spanwise width  $L_z^+$  using an arc-length continuation algorithm, while maintaining  $L_x^+$  and  $L_y^+$  the same. Solution curves are traced out and bifurcation points are identified. The  $(L_z^+, \Delta^+)$  bifurcation diagram is shown in figure 9(a), where  $\Delta^+ = dU^+/dy^+|_{y^+=0}$  is the wall shear rate of each solution.

In the reference domain  $\Omega$ , in which  $L_z^+ = 110$ ,  $PO_{A0L}$  is the edge state and  $EQ_{A1L}$  is the equilibrium solution embedded in the edge, as mentioned previously. Continuing  $PO_{A0L}$  to larger values of  $L_z^+$  (in brown), it forms a saddle-node bifurcation at  $L_z^+ \approx 136$  (as seen in the inset in figure 9a), beyond which it gains two more real unstable

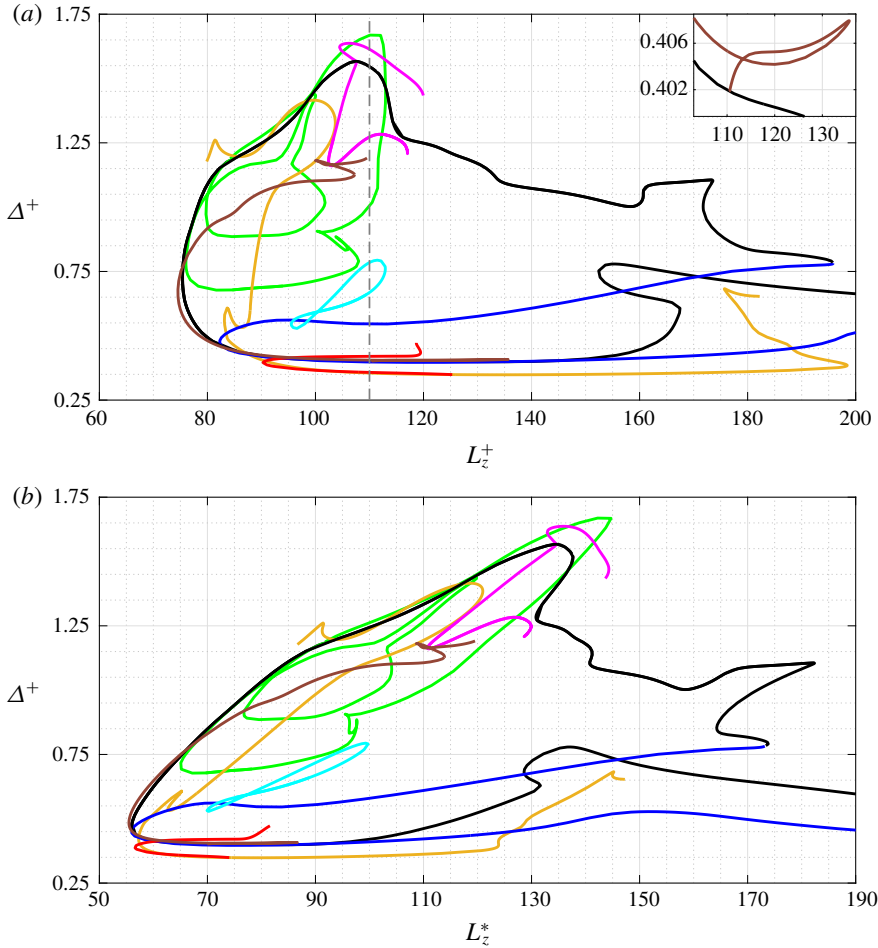


FIGURE 9. (Colour online) Wall shear rate of the invariant solutions,  $\Delta^+$ , as a function of the spanwise width; (a)  $L_z^+$  normalised by  $u_{\tau,r}$ , (b)  $L_z^*$  normalised by  $u_{\tau,e}$ . The grey dashed line represents the width of the reference domain  $\Omega$ . Brown line,  $PO_{A0L}$  &  $PO_{C0U}$ ; black line,  $EQ_{A1L}$  &  $EQ_{C1U}$ ; gold line,  $EQ_{A2}$ ; blue line,  $EQ_{A3L}$  &  $EQ_{B3U}$ ; red line,  $EQ_{A4L}$  &  $EQ_{B4U}$ ; green line,  $EQ_{B5L}$  &  $EQ_{C5U}$ ; cyan line,  $EQ_{B6L}$  &  $EQ_{B6U}$ ; pink line,  $EQ_{C7L}$  &  $EQ_{C7U}$ . The  $\Delta^+$  values of  $PO_{A0L}$  and  $PO_{C0U}$  are averages over the period  $T^+$ . The inset shows the subcritical Hopf bifurcation of  $EQ_{A1L}$ .

eigenvalues. It turns back to smaller values of  $L_z^+$  and at  $L_z^+ \approx 111$ , the periodic orbit collides with the  $EQ_{A1L}$  lower branch. Analysing the eigenvalues of  $EQ_{A1L}$  reveals that it is stable on the edge for  $L_z^+ > 111$  and unstable on the edge for  $L_z^+ < 111$ , indicating that this is a subcritical Hopf bifurcation. Continuing  $PO_{A0L}$  to smaller values of  $L_z^+$  instead, the drag begins to increase and it forms saddle-node bifurcation at  $L_z^+ \approx 74.5$ , the only solution to exist at this length scale. Above the bifurcation point, the drag increases substantially and after two further sharp saddle-node bifurcations, it reaches its maximum at the upper branch periodic orbit  $PO_{C0U}$ . The  $EQ_{A1L}$  state (in black) exhibits similar behaviour at smaller values of  $L_z^+$ , forming a saddle-node bifurcation at  $L_z^+ \approx 75.5$ . However, at larger values of  $L_z^+$ , the upper branch shows increasingly erratic behaviour until it turns sharply at  $L_z^+ \approx 196$ . The solution curve continues

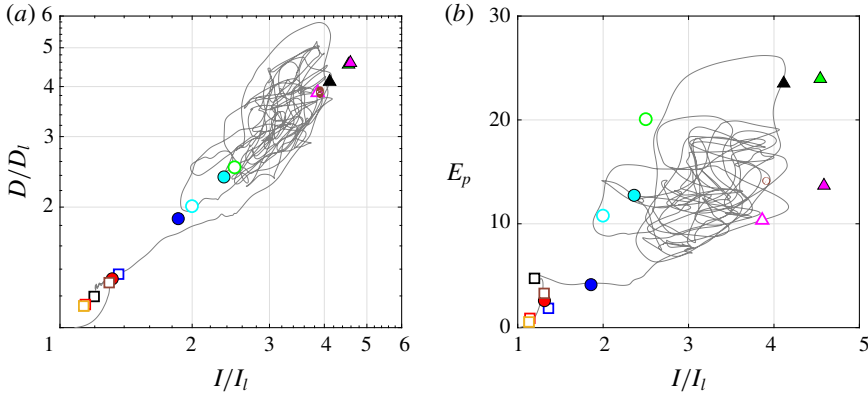


FIGURE 10. (Colour online) Phase portraits of a turbulent trajectory and the invariant solutions: (a) the  $(I/I_l, D/D_l)$  plane, where  $I_l$  and  $D_l$  represent the energy input and dissipation of the laminar state; (b) the  $(I/I_l, E_p)$  plane, where  $E_p$  is the kinetic energy deviation from the laminar state. Brown square & line,  $PO_{A0L}$  &  $PO_{C0U}$ ; black square & triangle,  $EQ_{A1L}$  &  $EQ_{C1U}$ ; gold square,  $EQ_{A2}$ ; blue square & circle,  $EQ_{A3L}$  &  $EQ_{B3U}$ ; red square & circle,  $EQ_{A4L}$  &  $EQ_{B4U}$ ; green circle & triangle,  $EQ_{B5L}$  &  $EQ_{C5U}$ ; cyan unfilled & filled circles,  $EQ_{B6L}$  &  $EQ_{B6U}$ ; pink unfilled & filled triangles,  $EQ_{C7L}$  &  $EQ_{C7U}$ . The  $I/I_l$ ,  $D/D_l$  and  $E_p$  values of  $PO_{A0L}$  are averages over the period  $T^+$ .

back down to smaller values of  $L_z^+$ , forming the upper branch on which  $EQ_{B3U}$  exists (in blue). The drag decreases through the saddle-node bifurcation point at  $L_z^+ \approx 82.5$  but is largely constant in the neighbourhood of the lower branch solution,  $EQ_{A3L}$ . Clearly, there is a relationship between these two pairs of equilibrium solutions. This is reinforced by the fact that the drag of  $EQ_{A1L}$  and  $EQ_{A3L}$  is almost identical over the interval  $90 < L_z^+ < 150$ .

The  $EQ_{B5L}$  and  $EQ_{C5U}$  states are also related to the above solution pairs, as mentioned in §3.1. Just above the bifurcation point of  $EQ_{C1U}$ , the number and magnitude of unstable eigenvalues increases significantly, meaning that the upper branch is highly unstable. A secondary solution curve emerges at  $L_z^+ \approx 84$  (in green), namely that of  $EQ_{C5U}$ , which is the solution with the highest drag in  $\Omega$ . Just above  $L_z^+ \approx 112$ , there is a sharp reduction in drag before the solution curve continues back to smaller values of  $L_z^+$  in the vicinity of the lower branch solution,  $EQ_{B5L}$ . At smaller values of  $L_z^+$  again, this solution curve exhibits erratic ‘looping’ behaviour, before it eventually rejoins the  $EQ_{C1U}$  branch from which it emerged.

The  $EQ_{A2}$  state (in gold) is the only solution without an upper branch counterpart in  $\Omega$ . The drag of the lower branch remains almost constant over the interval  $100 < L_z^+ < 190$  but increases as it approaches the cusp-like saddle-node bifurcation point at  $L_z^+ \approx 83$ . Along the upper branch, there is a substantial increase in drag before the solution curve turns again and continues back down to smaller values of  $L_z^+$ . Below  $L_z^+ \approx 80$ , the residual began to increase above the desired threshold so further continuation was abandoned. In contrast, the remaining three pairs of equilibria,  $EQ_{A4L}$  &  $EQ_{B4U}$  (in red),  $EQ_{B6L}$  &  $EQ_{B6U}$  (in cyan) and  $EQ_{C7L}$  &  $EQ_{C7U}$  (in pink), are all well-defined lower and upper branch pairs. However, the solution curves of each pair differ significantly. The  $EQ_{A4L}$  and  $EQ_{B4U}$  states have a parabolic-shaped curve, emerging in a saddle-node bifurcation at  $L_z^+ \approx 90$ , even though the difference in drag between the lower and upper branches is quite small. The  $EQ_{B6L}$  and  $EQ_{B6U}$

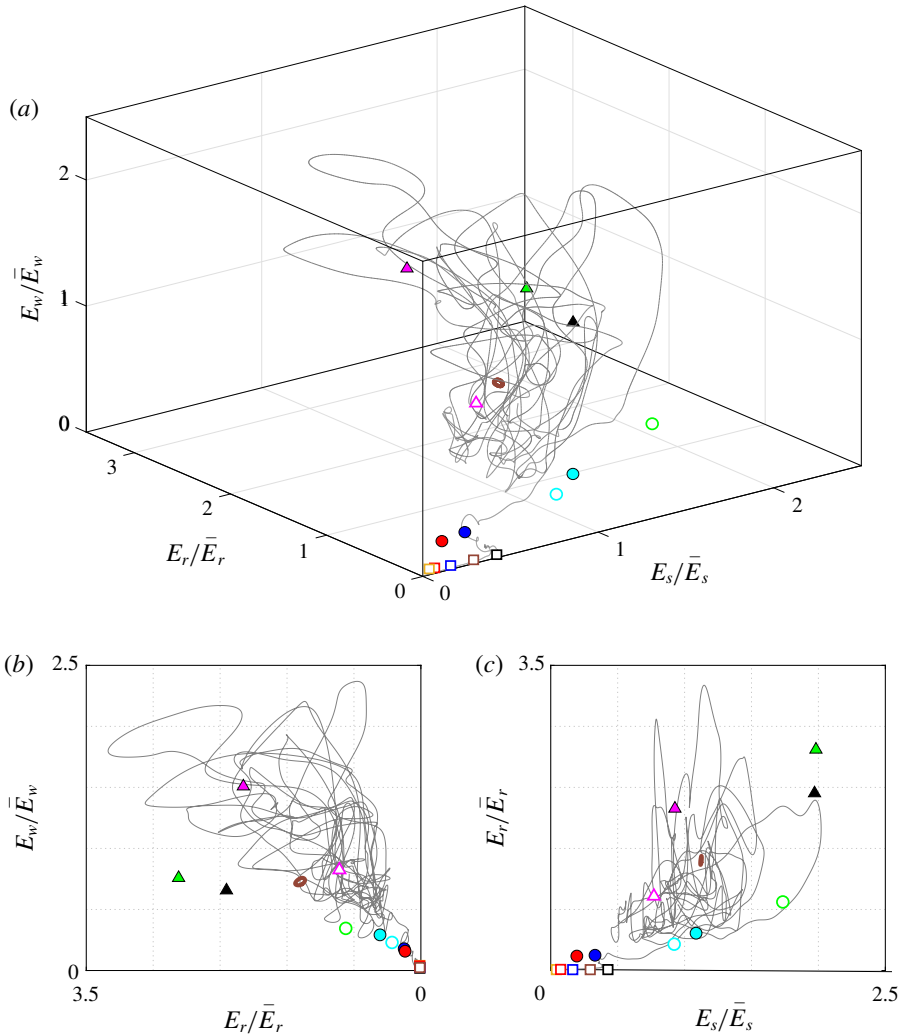


FIGURE 11. (Colour online) Phase portraits of a turbulent trajectory and the invariant solutions: (a)  $(E_s/\bar{E}_s, E_r/\bar{E}_r, E_w/\bar{E}_w)$  space, where  $E_s$ ,  $E_r$  and  $E_w$  represent the streak, roll and wave energy respectively, and  $\bar{\cdot}$  denotes the average in time while the flow remains turbulent; (b) the  $(E_r/\bar{E}_r, E_w/\bar{E}_w)$  plane; (c) the  $(E_s/\bar{E}_s, E_r/\bar{E}_r)$  plane. The symbols are identical to those used in figure 10.

states possess a unique lemniscate curve, while  $EQ_{C7L}$  and  $EQ_{C7U}$  have an almost rectangular-shaped curve. Another common feature of these three pairs of equilibria is that they only exist over a very limited interval of  $L_z^+$ , namely  $90 < L_z^+ < 125$ .

The bifurcation diagram in figure 9(a) also provides insight into the length scales of turbulent activity in the near-wall region. The  $PO_{A0L}$  state is the solution that exists at the smallest spanwise width,  $L_z^+ \approx 74.5$ , and no solutions exist below this value. As  $L_z^+$  increases, nearly all of the equilibrium solutions are born through saddle-node bifurcations, thirteen of which exist in  $\Omega$ . With the exception of  $EQ_{B3U}$ , all upper branch solutions achieve maximum drag in the interval  $100 < L_z^+ < 120$ , corresponding to the characteristic spacing of near-wall streaks (Robinson 1991). While the upper



branch solutions are much more sensitive to the spanwise width, the lower branch solutions show little variation in drag and even quasi-constant behaviour over moderate values of  $L_z^+$ . At the largest values of  $L_z^+$ , only a few lower branch solutions still exist. As an aside, the  $(L_z^*, \Delta^+)$  bifurcation diagram is shown in figure 9(b), where  $L_z^*$  is the spanwise width normalised with the friction velocity of the corresponding invariant solution,  $u_{\tau,e}$ . Under this rescaling, the bifurcation points of the solutions  $PO_{A0L}$ ,  $EQ_{A1L}$ ,  $EQ_{A2}$ ,  $EQ_{A3L}$  and  $EQ_{A4L}$  coincide at  $L_z^* \approx 55$ , similar to that of the high- $Re$  asymptotic state reported by Yang *et al.* (2019). The slight discrepancy is likely due to the 2:1 aspect ratio of the horizontal computational domain (i.e.  $L_x:L_z$ ) maintained in that work.

### 3.3. Phase portraits

Now that the connections between various invariant solutions have been determined, an approximation to the state space of near-wall turbulence can be constructed. This is the ultimate aim of the dynamical systems approach, namely how the position and stability of invariant solutions guide a chaotic turbulent trajectory through the state space. A particular phase portrait is usually chosen to exploit the inherent properties of invariant solutions or to shed light on a specific physical process. For example, if the total kinetic energy is defined as

$$E(t^+) = \frac{1}{2} \langle \mathbf{u}^+ \cdot \mathbf{u}^+ \rangle_{x^+,y^+,z^+}, \tag{3.4}$$

then its time derivative can be expressed as  $dE/dt^+ = I - D$ , where

$$I(t^+) = \left\langle u^+ \frac{\partial u^+}{\partial y^+} \Big|_{y^+=L_z^+} \right\rangle_{x^+,z^+}, \tag{3.5}$$

is the energy input and

$$D(t^+) = \left\langle \left( \frac{\partial u_i^+}{\partial x_j^+} \right)^2 \right\rangle_{x^+,y^+,z^+}, \tag{3.6}$$

is the energy dissipation. However, the energy conservation property of invariant solutions implies that  $dE/dt^+$  (or its average over the period  $T^+$  in the case of periodic orbits) is identically zero, hence  $I$  and  $D$  (or their average over  $T^+$ ) must be equal quantities. Denoting the energy input and dissipation of the laminar state by  $I_l$  and  $D_l$  respectively, the  $(I/I_l, D/D_l)$  phase portrait of a turbulent trajectory and the invariant solutions is shown in figure 10(a). The invariant solutions are positioned along the diagonal, while the turbulent trajectory oscillates around it in a chaotic manner and eventually relaminarises at late time. Introducing the deviation from the laminar state  $\mathbf{u}_p^+ = \mathbf{u}^+ - \mathbf{u}_l^+ = (u_p^+, v_p^+, w_p^+)$ , the perturbation kinetic energy may be defined as

$$E_p(t^+) = \frac{1}{2} \langle \mathbf{u}_p^+ \cdot \mathbf{u}_p^+ \rangle_{x^+,y^+,z^+}. \tag{3.7}$$

This quantity (or its average over  $T^+$ ) also remains constant for invariant solutions, thus allowing for the construction of an alternative phase portrait. The  $(I/I_l, E_p)$  phase portrait of the same turbulent trajectory and the invariant solutions is shown in figure 10(b). As expected, the energy input and perturbation kinetic energy of the



invariant solutions is positively correlated. The A, B and C grouping of solutions is also clearly visible in both phase portraits. The Group A solutions, represented by squares, are positioned closest to the laminar state, satisfying  $I/I_l = D/D_l < 1.4$  and  $E_p < 5$  (table 3). These solutions form a lower bound to the self-sustaining turbulent trajectory, consonant with the fact that  $PO_{A0L}$  is the edge state and  $EQ_{A1L}$  is embedded in the edge. In contrast, the Group C equilibria, represented by triangles, and periodic orbit are closer to the maximum values attained by the turbulent trajectory, with  $I/I_l = D/D_l > 3.8$ . The Group B equilibria, represented by circles, fill in the gap between the other two, closer to the mean turbulent state.

A particular phase portrait may also be chosen to investigate a specific physical process. In the case of near-wall turbulence, the relevant process is of course the self-sustaining process (Hamilton *et al.* 1995). It is therefore of interest to relate the relative equilibrium solutions and relative periodic orbits to the self-sustaining process, in order to study the state space dynamics in greater detail. In order to capture the three distinct stages, the self-sustaining process will be illustrated by a three-dimensional phase portrait. Following the approach of Lucas & Kerswell (2017), the kinetic energy of the streak, roll and wave are defined as

$$E_s(t^+) = \frac{1}{2} \langle \langle u_p^+ \rangle_{x^+}^2 \rangle_{y^+, z^+}, \quad (3.8)$$

$$E_r(t^+) = \frac{1}{2} \langle \langle v_p^+ \rangle_{x^+}^2 + \langle w_p^+ \rangle_{x^+}^2 \rangle_{y^+, z^+}, \quad (3.9)$$

and

$$E_w(t^+) = \frac{1}{2} \langle \langle \mathbf{u}_p^+ - \langle \mathbf{u}_p^+ \rangle_{x^+} \rangle_{x^+}^2 \rangle_{y^+, z^+}, \quad (3.10)$$

respectively, such that  $E_s + E_r + E_w = E_p$ . Since the streak energy is of higher order than that of the roll and wave, the above quantities are normalised by their mean turbulent values in the phase portraits in figure 11. The three-dimensional portrait is shown in figure 11(a), while the two-dimensional  $(E_r/\bar{E}_r, E_w/\bar{E}_w)$  and  $(E_s/\bar{E}_s, E_r/\bar{E}_r)$  portraits are shown in figures 11(b) and 11(c) respectively. It is immediately obvious that the invariant solutions are dispersed throughout the phase portrait, indicating that the solutions have very different dynamics.

The  $(E_s/\bar{E}_s, E_r/\bar{E}_r, E_w/\bar{E}_w)$  phase portrait allows for the clearest distinction between the three groups of solutions. The Group A solutions (squares) possess very little roll or wave energy, positioned almost at the origin of the  $(E_r/\bar{E}_r, E_w/\bar{E}_w)$  plane. They are positioned almost along the abscissa of the  $(E_s/\bar{E}_s, E_r/\bar{E}_r)$  plane, with  $EQ_{A1L}$  (the equilibrium solution embedded in the edge) showing greatest streak energy and  $EQ_{A2}$  (the solution with lowest drag) showing least. On the other hand, the high drag Group C equilibria (triangles) and periodic orbit possess the greatest roll and wave energy, corresponding to their high vorticity content. The Group B equilibria (circles) again bridge the gap, with moderately low values of both roll and wave energy. Interestingly, the Group B and C solutions are not distinguishable based on streak energy alone, given that strong streaky structures appear in the velocity field visualisations in both groups.

The above phase portraits also illustrate the interruption of the self-sustaining process and the consequent relaminarisation of the flow. At late time, the trajectory appears to escape from the turbulent state and enters the neighbourhood of the low energy states on the way to the laminar state. In particular, the trajectory appears to approach  $EQ_{B3U}$  then  $EQ_{A1L}$ , as seen in each of the  $(I/I_l, D/D_l)$ ,  $(I/I_l, E_p)$  and  $(E_s/\bar{E}_s, E_r/\bar{E}_r, E_w/\bar{E}_w)$  phase portraits. However,  $EQ_{A1L}$  is the equilibrium solution

embedded in the edge and other than its instability to the edge state, its only unstable eigendirection is transversal to the edge. In this case, the turbulent trajectory passes through the edge along the unstable manifold of  $EQ_{AIL}$ , exhibiting the characteristic decay of the roll energy. The turbulent trajectory then approaches the laminar state along the  $E_s$  axis, corresponding to the slow decay of the streak energy.

It must be pointed out that each phase portrait provides a limited description of the infinite-dimensional dynamical system that is turbulence. The dynamics of turbulence that lies in dimensions orthogonal to a given phase portrait will be omitted, hence important physical processes may be missed. The  $(I/I_l, D/D_l)$  and  $(I/I_l, E_p)$  phase portraits shown above are not without criticism (Budanur *et al.* 2017). For example, the edge is not recognisable as the boundary between the laminar and turbulent flow regimes. Neither  $PO_{AOL}$ , the edge state, nor  $EQ_{AIL}$ , the equilibrium solution embedded in the edge, have the lowest values of  $I/I_l$ ,  $D/D_l$  or  $E_p$  and several other equilibria appear to be positioned between them and the laminar state. In addition,  $EQ_{B4U}$  appears to be positioned closer to the Group A solutions, even though its velocity field is structurally very different to the solutions in that group. In order to gain a more thorough understanding of the state space of near-wall turbulence, the construction of phase portraits must be combined with the careful analysis of velocity fields, solution stability and bifurcation behaviour.

### 3.4. High- $Re$ asymptotic behaviour of equilibria

Following the model formulation in § 2, all results presented thus far have been scaled in inner units, where the domain dimensions  $(L_x^+, L_y^+, L_z^+)$  have been the only model parameters. By the definition of the system, its Reynolds number is of order unity. In this regime, the asymptotic description should follow Deguchi (2015). Of course, the same results can be rescaled in outer units for the purpose of studying the asymptotic behaviour in the limit of vanishing viscosity. In this case, the definition of a Reynolds number is required. Using the domain height  $L_y$  as the characteristic length scale, the laminar bulk velocity  $U_0$  as the characteristic velocity scale and the kinematic viscosity  $\nu$ , the Reynolds number can be defined as

$$Re = \frac{L_y U_0}{\nu}. \tag{3.11}$$

In outer units, the model parameters are therefore the streamwise length of the domain  $L_x/L_y$ , the spanwise width of the domain  $L_z/L_y$  and the Reynolds number  $Re$ . In the current configuration, the values of these parameters are  $L_x/L_y \approx 3.56$ ,  $L_z/L_y \approx 1.22$  and  $Re = 1250$ . Given the definition of a Reynolds number, it is of interest to study the asymptotic development of the relative equilibrium solutions at high  $Re$  with  $L_x/L_y$  and  $L_z/L_y$  fixed as above. In particular, the scaling of the equilibria with  $Re$  will be examined and compared to established theories at high Reynolds number (Hall & Sherwin 2010), since this will provide valuable information about the asymptotic structure of the equilibrium solutions in the near-wall computational domain. To this end, the deviation from the laminar state  $\mathbf{u}_p = (\mathbf{u} - \mathbf{u}_l)/U_0$  is reintroduced and the kinetic energy of the streak and roll are defined analogous to (3.8) and (3.9) respectively. The wave velocity field is subsequently defined as

$$(\mathbf{u}_w, v_w, w_w) = \mathbf{u}_p - \langle \mathbf{u}_p \rangle_x, \tag{3.12}$$

and the energy of the first and second streamwise modes of the wave as

$$E_{w1} = \frac{1}{2} \langle \hat{u}_w^2(\pm 1, y, 0) + \hat{v}_w^2(\pm 1, y, 0) + \hat{w}_w^2(\pm 1, y, 0) \rangle_y, \tag{3.13}$$

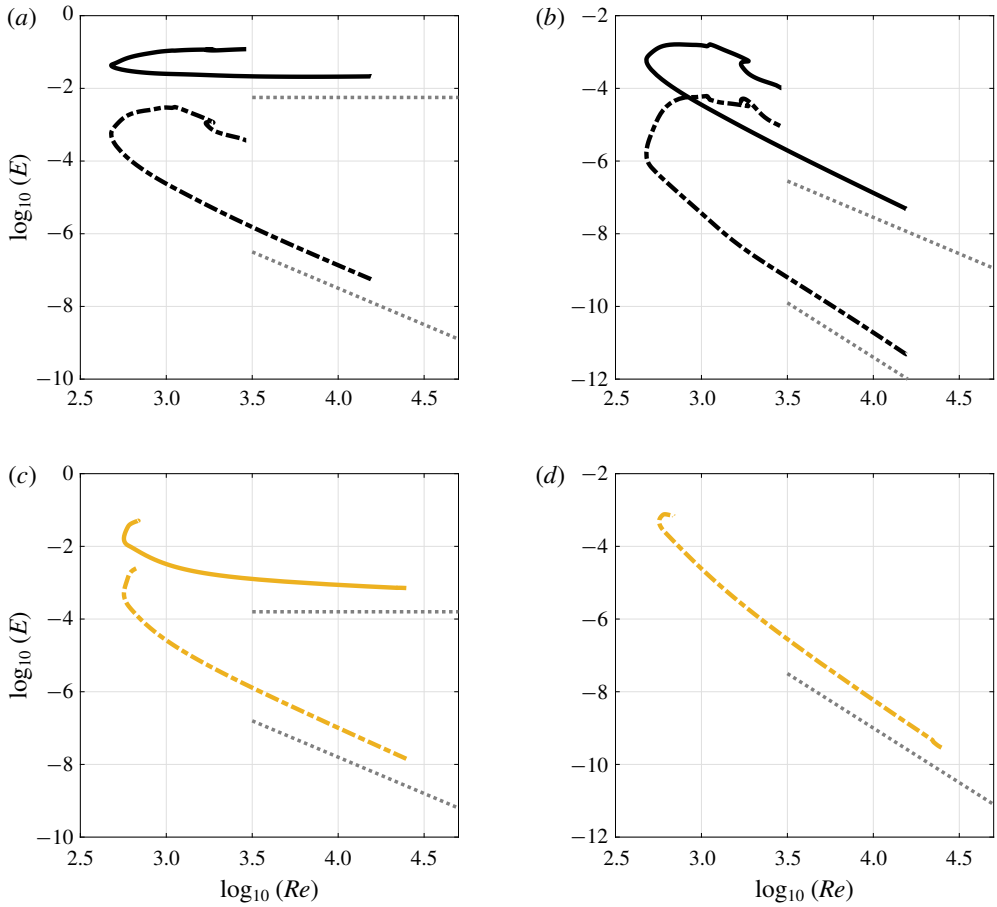


FIGURE 12. For caption see next page.

and

$$E_{w2} = \frac{1}{2} \langle \hat{u}_w^2(\pm 2, y, 0) + \hat{v}_w^2(\pm 2, y, 0) + \hat{w}_w^2(\pm 2, y, 0) \rangle_y, \tag{3.14}$$

where  $\widehat{\cdot}$  denotes the Fourier transform.

The scaling of  $EQ_{A1L}$ ,  $EQ_{A2}$ ,  $EQ_{A3L}$  and  $EQ_{A4L}$  with  $Re$  is shown in figure 12, together with their upper branch counterparts  $EQ_{C1U}$ ,  $EQ_{B3U}$  and  $EQ_{B4U}$ . The streak and roll energy are shown in (a,c,e,g) and the energy of the first and second streamwise modes of the wave are shown in (b,d,f,h). The  $EQ_{A1L}$ ,  $EQ_{A3L}$  and  $EQ_{A4L}$  states all exhibit the characteristic vortex–wave interaction (VWI) scaling, where  $E_s \sim Re^0$ ,  $E_r \sim Re^{-2}$ ,  $E_{w1} \sim Re^{-2}$  and  $E_{w2} \sim Re^{-3}$  (Hall & Sherwin 2010). This result is not surprising, given that the Group A solutions possess very little roll or wave energy relative to streak energy, as seen in figure 11. The  $EQ_{A2}$  state exhibits similar behaviour, except that the energy of the fundamental streamwise mode of the wave is approximately zero and hence not shown. The upper branch solutions  $EQ_{C1U}$ ,  $EQ_{B3U}$  and  $EQ_{B4U}$  could not be continued to as high values of the Reynolds number due to the increasing instability of equilibria at high  $Re$ . The relative equilibrium solutions not included in figure 12 either could not be continued or collided in saddle-node bifurcations at higher values of  $Re$ .

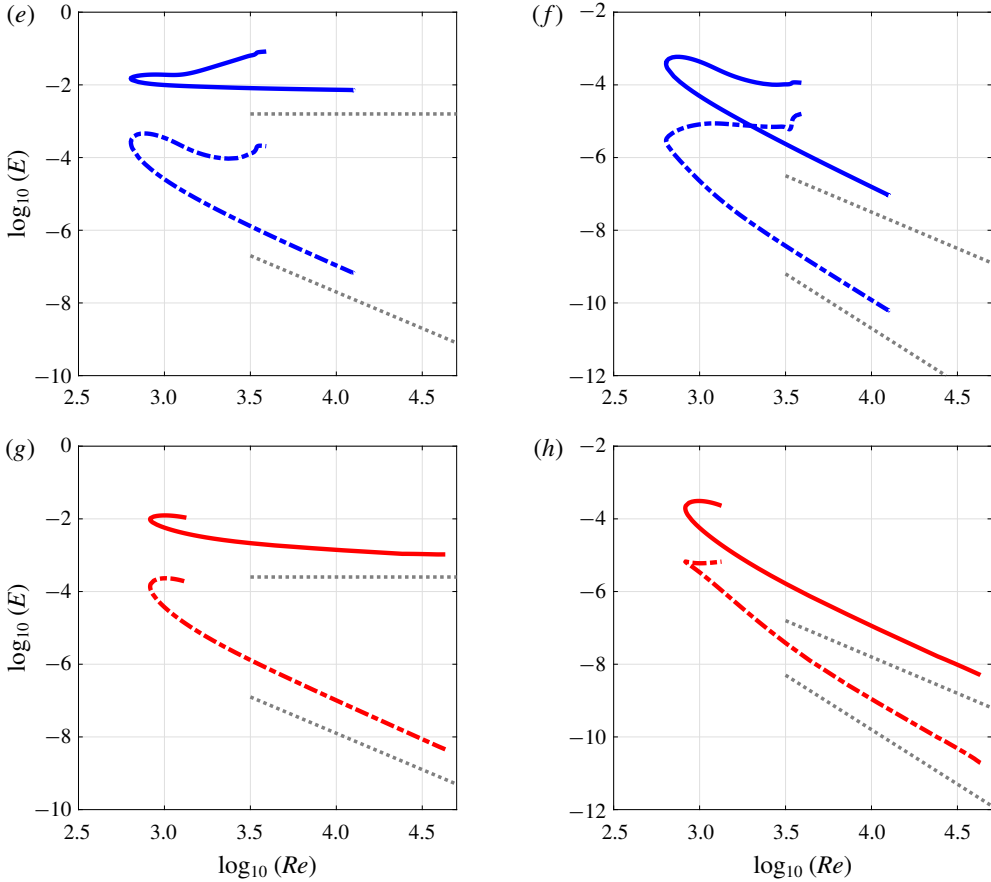


FIGURE 12 (cntd). (Colour online) Scaling of (a,b)  $EQ_{A1L}$ , (c,d)  $EQ_{A2}$ , (e,f)  $EQ_{A3L}$  and (g,h)  $EQ_{A4L}$  with  $Re$ ; (a,c,e,g) solid lines,  $E_s$ , dash-dotted lines,  $E_r$ ; (b,d,f,h) solid lines,  $E_{w1}$ , dash-dotted lines,  $E_{w2}$ . The grey dotted lines represent the VWI scaling;  $E_s \sim Re^0$ ,  $E_r \sim Re^{-2}$ ,  $E_{w1} \sim Re^{-2}$  and  $E_{w2} \sim Re^{-3}$ .

In addition to the characteristic Reynolds number scaling, VWI states are distinguishable by their velocity field structure. As shown in Hall & Sherwin (2010), the roll equations are driven by the Reynolds stresses of the wave, defined as

$$F_y = - \left\langle u_w \frac{\partial v_w}{\partial x} + v_w \frac{\partial v_w}{\partial y} + w_w \frac{\partial v_w}{\partial z} \right\rangle_x, \quad (3.15)$$

and

$$F_z = - \left\langle u_w \frac{\partial w_w}{\partial x} + v_w \frac{\partial w_w}{\partial y} + w_w \frac{\partial w_w}{\partial z} \right\rangle_x. \quad (3.16)$$

However, in the limit of  $Re \rightarrow \infty$ , the wave equations become singular in the critical layer, where the mean streamwise velocity and phase speed are equal,  $U(y, z) = c_x$ . Hence, VWI states exhibit the localisation of the wave forcing,  $F(y, z) = \sqrt{F_y^2 + F_z^2}$ ,

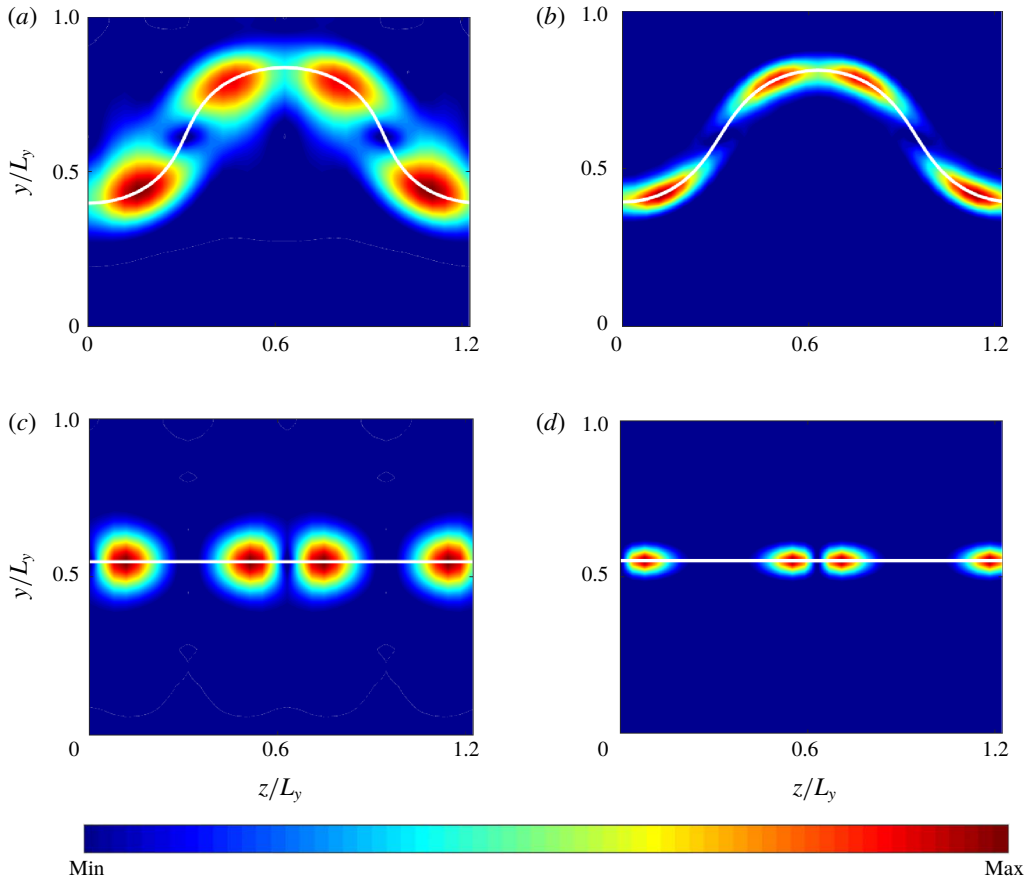


FIGURE 13. For caption see next page.

around the critical layer at high Reynolds number. The critical layer position and wave forcing of  $EQ_{A1L}$ ,  $EQ_{A2}$ ,  $EQ_{A3L}$  and  $EQ_{A4L}$  is shown in figure 13, at  $Re = 1250$  (a,c,e,g) and  $Re = 12500$  (b,d,f,h). At lower Reynolds number, the wave forcing is more spatially extensive, affecting a large area surrounding the critical layer. Maximum values are attained in the critical layer with gradual spatial decay in the outer region. However, as the Reynolds number increases, the spatial extent of the wave forcing decreases and in each case, it is confined to the critical layer in the limit of  $Re \rightarrow \infty$ . In particular,  $EQ_{A2}$  possesses a flat critical layer, like EQ7 in Gibson *et al.* (2009) (see also Deguchi, Hall & Walton 2013).

The  $EQ_{A1L}$  state, which appears to be the analogue of Nagata's lower branch solution, has been exemplified as the canonical VWI state (Hall & Sherwin 2010). However, it has been shown above that two new equilibrium solutions exhibit VWI scaling and the localisation of wave forcing in the critical layer, namely  $EQ_{A3L}$  and  $EQ_{A4L}$ . Each of these solutions is structurally similar, with small cross-streamwise velocity fluctuations relative to streamwise velocity fluctuations. This is highlighted by the position of the Group A solutions close to the origin of the  $(E_r/\bar{E}_r, E_w/\bar{E}_w)$  phase plane in figure 11(b). The primary difference between the three states is their wall-normal localisation, where  $EQ_{A3L}$  appears to be fully attached to the wall,  $EQ_{A4L}$  in the domain centre and  $EQ_{A1L}$  along the upper boundary. The VWI states reside

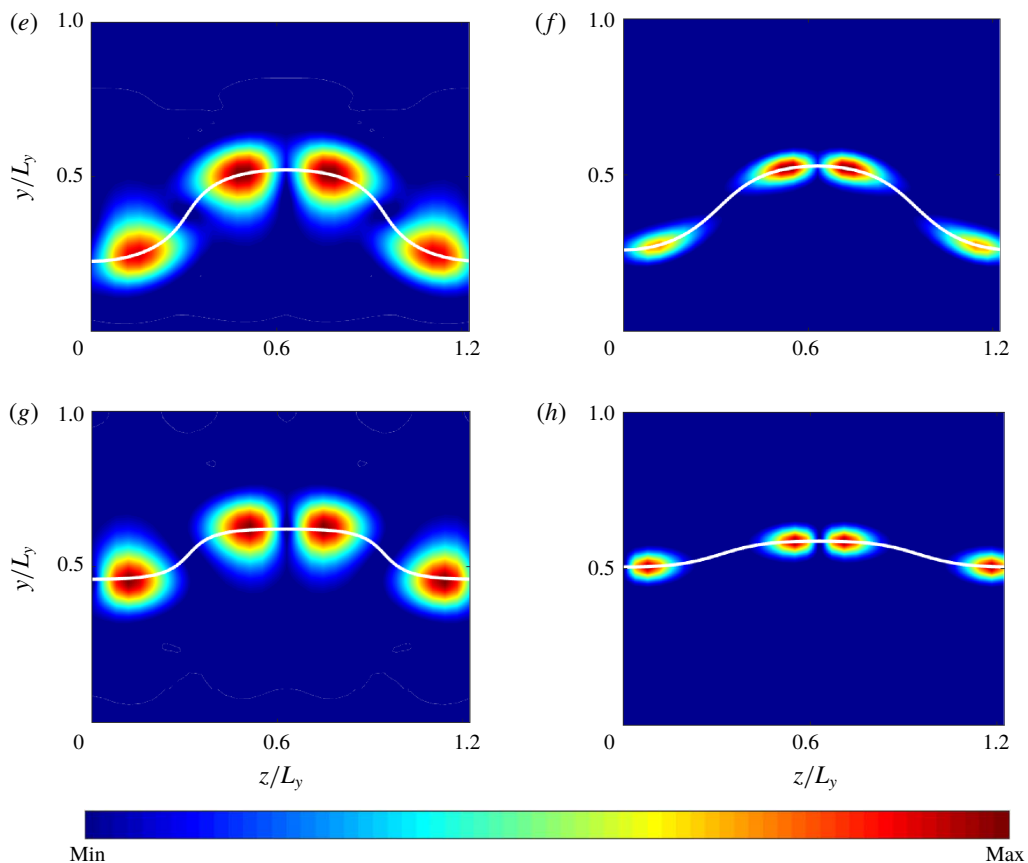


FIGURE 13 (cntd.). (Colour online) Wave-induced forcing,  $F(y, z)$ , of (a,b)  $EQ_{A1L}$ , (c,d)  $EQ_{A2}$ , (e,f)  $EQ_{A3L}$  and (g,h)  $EQ_{A4L}$ ; (a,c,e,g)  $Re = 1250$ ; (b,d,f,h)  $Re = 12\,500$ . The white line represents the critical layer position,  $U(y, z) = c_x$ .

in the same neighbourhood of the state space of near-wall turbulence. As lower branch solutions, they are characterised by drag rates well below the turbulent mean, relatively high phase speeds and low energy input and dissipation rates (table 3). They are the most stable equilibrium solutions, each possessing three unstable eigenvalues, consonant with their position within or proximity to the edge. In addition, the VWI states are among the first solutions to emerge via saddle-node bifurcation in the  $(L_z^*, \Delta^+)$  bifurcation diagram in figure 9(b). The bifurcation point appears to be  $L_z^* \approx 55$ , below which only the laminar state exists, indicating their relevance to the transition to turbulence.

However, it must be pointed out that the VWI states only account for a small subset of the invariant solutions presented above. Since they form a lower bound to the turbulent trajectory in terms of drag, energy input and perturbation kinetic energy, the VWI states fail to capture fully turbulent dynamics. The Group B equilibria best represent the statistics and structure of the mean turbulent state, featuring high- and low-speed streaks and quasi-streamwise vortices. In particular,  $EQ_{B5L}$  has wall shear rate  $\Delta^+ \approx 1$  and has a similar velocity profile to that of the reference simulation (figure 3). Together with  $EQ_{B6U}$ , it appears close to the mean turbulent values of

the energy input, dissipation and perturbation kinetic energy in figure 10, and streak energy in figure 11. The Group C solutions are the most ‘turbulent’, in the sense that they exhibit highly wavy streaks and significant vortical content. They appear to form an upper bound to the turbulent trajectory in terms of drag, energy input and dissipation and roll energy, lying close to the extremal turbulent trajectories in figures 10(a) and 11(c). Consequently, these invariant solutions are extremely unstable. For example,  $EQ_{CTU}$  is the most unstable equilibrium solution in  $\Omega$ , with an incredible 63-dimensional unstable manifold, and  $PO_{COU}$  is the most unstable periodic orbit, with a 47-dimensional unstable manifold. However, the Group C solutions are the only ones to attain wave energy values close to the turbulent mean in figure 11(b) and they also move with phase speeds  $12 < c_x^+ < 14$ , comparable with the advection velocity of the near-wall coherent structures observed in numerical experiments (Kim & Hussain 1993). Clearly, the solutions of Group B and C play an important role in describing the full dynamics of near-wall turbulence.

#### 4. Conclusion

In this work, a shear stress-driven flow is introduced as a model of independent near-wall turbulence as  $Re_\tau \rightarrow \infty$ . The system is governed by the unit Reynolds number Navier–Stokes equations, which are valid throughout the mesolayer. A horizontally uniform shear stress is imposed at the upper boundary of the domain so as to satisfy the mean momentum equation. This model is applicable to various parallel shear flows, including turbulent Couette flow, Poiseuille flow and Hagen–Poiseuille flow, provided that  $L_x^+, L_y^+, L_z^+ \sim \sqrt{Re_\tau}$ . In addition, shear stress-driven flow is employed as a model of wind blowing over a body of water, hence the results presented here are also relevant in physical oceanography. The shear stress-driven flow model is validated against damped Couette flow and there is excellent agreement between the velocity statistics and spectra for  $y^+ < 40$ . Above this point, the mean streamwise velocity and streamwise velocity fluctuations are slightly overestimated, while the wall-normal and spanwise velocity fluctuations are slightly underestimated. Therefore, the shear stress-driven flow model can be said to describe the universal part of near-wall turbulence, which provides a means to study the flow dynamics and multiple-scale interaction unimpeded by the presence of an upper wall.

A near-wall flow domain of similar size to the minimal unit is analysed from a dynamical systems perspective. The edge exhibits both stationary and time-periodic behaviour, from which a relative equilibrium solution and a relative periodic orbit were computed. Fifteen invariant solutions are presented in total, which can be divided into three groups based on their physical properties. Through continuation in the spanwise width  $L_z^+$ , the bifurcation behaviour of the solutions is investigated and it is found that most emerge via saddle-node bifurcations in the interval  $70 < L_z^+ < 100$ . Furthermore, the upper branch solutions achieve maximum wall shear rate in the interval  $100 < L_z^+ < 120$ , corresponding to the characteristic spacing of near-wall streaks. When the spanwise width is instead normalised by the friction velocity of the computed solution, the bifurcation points of all Group A solutions coincide at  $L_z^* \approx 55$ , similar to the results obtained by Yang *et al.* (2019).

The present study is analogous to that of Jiménez & Simens (2001) but with several key differences. Firstly, the shear stress-driven flow model allows for the simulation of autonomous near-wall turbulence without the need for damping functions of the form (2.11). Damped flow simulations require a greater number of grid points, many



of which support only laminar flow, and the omission of these greatly improves the computational cost. Furthermore, the flow can be studied without consideration as to whether the precise form of the damping function will affect the dynamics. Secondly, the simulations in Jiménez & Simens (2001) were performed with constant volumetric flux maintained by a pressure gradient, resulting in the  $-y^+/Re_\tau$  term in the mean momentum equation (2.3). Given the simulation parameters, however, this term is an  $O(1)$  quantity and so the results of that study apply more directly to turbulent Poiseuille flow. Finally, the invariant solution in Jiménez & Simens (2001) is not computed explicitly and is only identifiable at low values of the mask height  $\delta_1^+$ . Above  $\delta_1^+ \approx 70$ , only chaotic turbulent flow is observed, in contrast to the fifteen explicitly computed invariant solutions presented in the current work for wall-normal domain height  $L_y^+ = 90$ .

The computation of the invariant solutions of the shear stress-driven flow model and their linear stability analysis allows for the construction of the state space of near-wall turbulence. The chaotic turbulent trajectory and invariant solutions are visualised in several phase portraits, including the energy input and dissipation plane, and streak, roll and wave energy space. The Group A solutions, three of which exhibit the characteristic vortex–wave interaction scaling at high- $Re$ , are characterised by low energy input and dissipation rates, relatively high phase speeds and few unstable eigenvalues, consonant with their proximity to the edge. While the Group A solutions form a lower bound to the turbulent trajectory, the Group B equilibria best represent the statistics and structure of the mean turbulent state, featuring high- and low-speed streaks and quasi-streamwise vortices. The Group C solutions appear to form an upper bound to the turbulent trajectory in terms of drag, energy input and dissipation and roll energy, and hence are extremely unstable. Though they do not exist at high values of  $Re$ , the Group B and C solutions play an important role in describing the full dynamics of near-wall turbulence.

The statistical results and invariant solutions presented in this work have all been computed in minimal ( $L_z^+ \approx 110$ ) near-wall ( $L_y^+ \approx 90$ ) flow domains, which only allow for the simulation of near-wall energy-containing structures at a single integral length scale (Jiménez & Moin 1991). However, the extent of the mesolayer increases as the friction Reynolds number increases as  $y_{max}^+ \sim \sqrt{Re_\tau}$ , meaning that at extremely high Reynolds numbers, the mesolayer encompasses a hierarchy of scales – not just one. Therefore, the governing equations (2.5) and (2.6) are valid for arbitrary values of the domain dimensions ( $L_x^+, L_y^+, L_z^+$ ), under the assumption that the friction Reynolds number is sufficiently high. Once the spanwise width of the domain exceeds  $L_z^+ \simeq 200$ , then energy-containing structures at two integral length scales ( $\lambda_z^+ \simeq 100, 200$ ) will be present, due to the periodic boundary condition in the spanwise direction. In such a flow domain, the interaction between the large- and small-scale structures will alter the turbulent dynamics, in contrast to the isolated single-scale turbulence analysed here. This study is only the first step in the investigation of multi-scale mesolayer turbulence.

## REFERENCES

- AFZAL, N. 1982 Fully developed turbulent flow in a pipe: an intermediate layer. *Ingenieur-Archiv* **52** (6), 355–377.
- AFZAL, N. 1984 Mesolayer theory for turbulent flows. *AIAA J.* **22** (3), 437–439.
- AGOSTINI, L. & LESCHZINER, M. 2016 Predicting the response of small-scale near-wall turbulence to large-scale outer motions. *Phys. Fluids* **28** (1), 015107.

- BARKLEY, D. 2016 Theoretical perspective on the route to turbulence in a pipe. *J. Fluid Mech.* **803**, P1.
- BEWLEY, T. R. 2014 *Numerical Renaissance: Simulation, Optimization and Control*. Renaissance Press.
- BUDANUR, N. B., SHORT, K. Y., FARAZMAND, M., WILLIS, A. P. & CVITANOVIĆ, P. 2017 Relative periodic orbits form the backbone of turbulent pipe flow. *J. Fluid Mech.* **833**, 274–301.
- CASSINELLI, A., DE GIOVANETTI, M. & HWANG, Y. 2017 Streak instability in near-wall turbulence revisited. *J. Turbul.* **18** (5), 443–464.
- CHO, M., HWANG, Y. & CHOI, H. 2018 Scale interactions and spectral energy transfer in turbulent channel flow. *J. Fluid Mech.* **854**, 474–504.
- DEGUCHI, K. 2015 Self-sustained states at Kolmogorov microscale. *J. Fluid Mech.* **781**, R6.
- DEGUCHI, K., HALL, P. & WALTON, A. 2013 The emergence of localized vortex–wave interaction states in plane Couette flow. *J. Fluid Mech.* **721**, 58–85.
- ECKHARDT, B. & ZAMMERT, S. 2018 Small scale exact coherent structures at large Reynolds numbers in plane Couette flow. *Nonlinearity* **31** (2), R66.
- FALLER, A. J. 1971 Oceanic turbulence and the Langmuir circulations. *Annu. Rev. Ecol. Systematics* **2** (1), 201–236.
- FUKAGATA, K., IWAMOTO, K. & KASAGI, N. 2002 Contribution of Reynolds stress distribution to the skin friction in wall-bounded flows. *Phys. Fluids* **14** (11), L73–L76.
- GIBSON, J. F., HALCROW, J. & CVITANOVIĆ, P. 2009 Equilibrium and travelling-wave solutions of plane Couette flow. *J. Fluid Mech.* **638**, 243–266.
- DE GIOVANETTI, M., SUNG, H. J. & HWANG, Y. 2017 Streak instability in turbulent channel flow: the seeding mechanism of large-scale motions. *J. Fluid Mech.* **832**, 483–513.
- HALL, P. & SHERWIN, S. 2010 Streamwise vortices in shear flows: harbingers of transition and the skeleton of coherent structures. *J. Fluid Mech.* **661**, 178–205.
- HAMILTON, J. M., KIM, J. & WALEFFE, F. 1995 Regeneration mechanisms of near-wall turbulence structures. *J. Fluid Mech.* **287**, 317–348.
- HUTCHINS, N. & MARUSIC, I. 2007 Large-scale influences in near-wall turbulence. *Phil. Trans. R. Soc. Lond. A* **365** (1852), 647–664.
- HWANG, Y. 2013 Near-wall turbulent fluctuations in the absence of wide outer motions. *J. Fluid Mech.* **723**, 264–288.
- HWANG, Y. 2015 Statistical structure of self-sustaining attached eddies in turbulent channel flow. *J. Fluid Mech.* **767**, 254–289.
- HWANG, Y. 2016 Mesolayer of attached eddies in turbulent channel flow. *Phys. Rev. Fluids* **1** (6), 064401.
- HWANG, Y. & BENGANA, Y. 2016 Self-sustaining process of minimal attached eddies in turbulent channel flow. *J. Fluid Mech.* **795**, 708–738.
- HWANG, Y. & COSSU, C. 2010 Self-sustained process at large scales in turbulent channel flow. *Phys. Rev. Lett.* **105** (4), 044505.
- HWANG, Y., WILLIS, A. P. & COSSU, C. 2016 Invariant solutions of minimal large-scale structures in turbulent channel flow for  $Re_\tau$  up to 1000. *J. Fluid Mech.* **802**, R1.
- JIMÉNEZ, J., DEL ALAMO, J. C. & FLORES, O. 2004 The large-scale dynamics of near-wall turbulence. *J. Fluid Mech.* **505**, 179–199.
- JIMÉNEZ, J., KAWAHARA, G., SIMENS, M. P., NAGATA, M. & SHIBA, M. 2005 Characterization of near-wall turbulence in terms of equilibrium and ‘bursting’ solutions. *Phys. Fluids* **17** (1), 015105.
- JIMÉNEZ, J. & MOIN, P. 1991 The minimal flow unit in near-wall turbulence. *J. Fluid Mech.* **225**, 213–240.
- JIMÉNEZ, J. & PINELLI, A. 1999 The autonomous cycle of near-wall turbulence. *J. Fluid Mech.* **389**, 335–359.
- JIMÉNEZ, J. & SIMENS, M. P. 2001 Low-dimensional dynamics of a turbulent wall flow. *J. Fluid Mech.* **435**, 81–91.
- KAWAHARA, G. & KIDA, S. 2001 Periodic motion embedded in plane Couette turbulence: regeneration cycle and burst. *J. Fluid Mech.* **449**, 291–300.

- KIM, J. & HUSSAIN, F. 1993 Propagation velocity of perturbations in turbulent channel flow. *Phys. Fluids A* **5** (3), 695–706.
- KIM, K. C. & ADRIAN, R. J. 1999 Very large-scale motion in the outer layer. *Phys. Fluids* **11** (2), 417–422.
- KOVASZNAVY, L. S. G., KIBENS, V. & BLACKWELDER, R. F. 1970 Large-scale motion in the intermittent region of a turbulent boundary layer. *J. Fluid Mech.* **41** (2), 283–325.
- LEE, M. J., KIM, J. & MOIN, P. 1990 Structure of turbulence at high shear rate. *J. Fluid Mech.* **216**, 561–583.
- LEIBOVICH, S. 1983 The form and dynamics of Langmuir circulations. *Annu. Rev. Fluid Mech.* **15** (1), 391–427.
- LONG, R. R. & CHEN, T.-C. 1981 Experimental evidence for the existence of the ‘mesolayer’ in turbulent systems. *J. Fluid Mech.* **105**, 19–59.
- LUCAS, D. & KERSWELL, R. 2017 Sustaining processes from recurrent flows in body-forced turbulence. *J. Fluid Mech.* **817**, R3.
- LUSTRO, J. R. T., KAWAHARA, G., VAN VEEN, L., SHIMIZU, M. & KOKUBU, H. 2019 The onset of transient turbulence in minimal plane Couette flow. *J. Fluid Mech.* **862**, R2.
- MARUSIC, I., BAARS, W. J. & HUTCHINS, N. 2017 Scaling of the streamwise turbulence intensity in the context of inner-outer interactions in wall turbulence. *Phys. Rev. Fluids* **2** (10), 100502.
- MARUSIC, I. & KUNKEL, G. J. 2003 Streamwise turbulence intensity formulation for flat-plate boundary layers. *Phys. Fluids* **15** (8), 2461–2464.
- MARUSIC, I., MONTY, J. P., HULTMARK, M. & SMITS, A. J. 2013 On the logarithmic region in wall turbulence. *J. Fluid Mech.* **716**, R3.
- MATHIS, R., HUTCHINS, N. & MARUSIC, I. 2009 Large-scale amplitude modulation of the small-scale structures in turbulent boundary layers. *J. Fluid Mech.* **628**, 311–337.
- NAGATA, M. 1990 Three-dimensional finite-amplitude solutions in plane Couette flow: bifurcation from infinity. *J. Fluid Mech.* **217**, 519–527.
- ORSZAG, S. A. 1971 Accurate solution of the Orr–Sommerfeld stability equation. *J. Fluid Mech.* **50** (4), 689–703.
- ROBINSON, S. K. 1991 Coherent motions in the turbulent boundary layer. *Annu. Rev. Fluid Mech.* **23** (1), 601–639.
- ROMANOV, V. A. 1973 Stability of plane-parallel Couette flow. *Funct. Anal. Appl.* **7** (2), 137–146.
- SCHNEIDER, T. M., ECKHARDT, B. & YORKE, J. A. 2007 Turbulence transition and the edge of chaos in pipe flow. *Phys. Rev. Lett.* **99** (3), 034502.
- SCHNEIDER, T. M., GIBSON, J. F., LAGHA, M., DE LILLO, F. & ECKHARDT, B. 2008 Laminar-turbulent boundary in plane Couette flow. *Phys. Rev. E* **78** (3), 037301.
- SCHOPPA, W. & HUSSAIN, F. 2002 Coherent structure generation in near-wall turbulence. *J. Fluid Mech.* **453**, 57–108.
- SEKIMOTO, A., DONG, S. & JIMÉNEZ, J. 2016 Direct numerical simulation of statistically stationary and homogeneous shear turbulence and its relation to other shear flows. *Phys. Fluids* **28** (3), 035101.
- SKUFCJA, J. D., YORKE, J. A. & ECKHARDT, B. 2006 Edge of chaos in a parallel shear flow. *Phys. Rev. Lett.* **96** (17), 174101.
- SREENIVASAN, K. R. & SAHAY, A. 1997 The persistence of viscous effects in the overlap region, and the mean velocity in turbulent pipe and channel flows. In *Self-Sustaining Mechanisms of Wall Turbulence* (ed. R. Panton), pp. 253–272. Computational Mechanics Publications.
- TALLURU, K. M., BAIDYA, R., HUTCHINS, N. & MARUSIC, I. 2014 Amplitude modulation of all three velocity components in turbulent boundary layers. *J. Fluid Mech.* **746**, R1.
- THORPE, S. A. 2004 Langmuir circulation. *Annu. Rev. Fluid Mech.* **36**, 55–79.
- TOMKINS, C. D. & ADRIAN, R. J. 2003 Spanwise structure and scale growth in turbulent boundary layers. *J. Fluid Mech.* **490**, 37–74.
- TOWNSEND, A. A. 1980 *The Structure of Turbulent Shear Flow*. Cambridge University Press.
- VISWANATH, D. 2007 Recurrent motions within plane Couette turbulence. *J. Fluid Mech.* **580**, 339–358.

- VISWANATH, D. 2009 The critical layer in pipe flow at high Reynolds number. *Phil. Trans. R. Soc. Lond. A* **367** (1888), 561–576.
- WALEFFE, F. 1997 On a self-sustaining process in shear flows. *Phys. Fluids* **9** (4), 883–900.
- WALEFFE, F. 1998 Three-dimensional coherent states in plane shear flows. *Phys. Rev. Lett.* **81** (19), 4140.
- WALEFFE, F. 2001 Exact coherent structures in channel flow. *J. Fluid Mech.* **435**, 93–102.
- WALEFFE, F. 2003 Homotopy of exact coherent structures in plane shear flows. *Phys. Fluids* **15** (6), 1517–1534.
- WEI, T., FIFE, P., KLEWICKI, J. & MCMURTRY, P. 2005 Properties of the mean momentum balance in turbulent boundary layer, pipe and channel flows. *J. Fluid Mech.* **522**, 303–327.
- WILLIS, A. P., CVITANOVIĆ, P. & AVILA, M. 2013 Revealing the state space of turbulent pipe flow by symmetry reduction. *J. Fluid Mech.* **721**, 514–540.
- YANG, Q., WILLIS, A. P. & HWANG, Y. 2018 Energy production and self-sustained turbulence at the kolmogorov scale in Couette flow. *J. Fluid Mech.* **834**, 531–554.
- YANG, Q., WILLIS, A. P. & HWANG, Y. 2019 Exact coherent states of attached eddies in channel flow. *J. Fluid Mech.* **862**, 1029–1059.